https://doi.org/10.1016/j.compfluid.2018.09.002

# A Lattice Boltzmann model for thermal non-Newtonian fluid flows through porous media

GH. R. Kefayati [a,*], H. Tang [b], A. Chan [a], X. Wang [a]

[a] *School of Engineering and ICT, University of Tasmania, Hobart, Tasmania, Australia*

[b] *Department of Mechanical Engineering, The Hong Kong Polytechnic University, Kowloon, Hong Kong*

---

## Abstract

Following recent studies by Huilgol and Kefayati [1,2], that developed a thermal Lattice Boltzmann method for different non-Newtonian fluids, we propose, in this paper, a general lattice Boltzmann method for thermal incompressible non-Newtonian fluids through porous media. Since no restrictions are placed on the constitutive equations in this method, the theoretical development can be applied to all fluids, whether they be Newtonian, or power law fluids, or viscoelastic and Bingham fluids. To validate the accuracy of the method, natural convection in a porous cavity was studied and compared with previous studies. Next, we employ the model to simulate natural convection of power-law and Bingham fluids in a porous cavity.

*Key words:* Non-Newtonian fluid, Porous media, Natural convection, LBM

---

## 1 Introduction

In numerous engineering areas through porous media , e.g., petroleum engineering, paper manufacturing, composite manufacturing, food industries, ceramic processing, enhanced oil recovery, filtration, liquid composite molding,

---

* Corresponding author. Dr. Gholamreza Kefayati (GH. R. Kefayati)
*Email addresses:* `gholamrezakefayati@gmail.com`, `gholamreza.kefayati@utas.edu.au` (GH. R. Kefayati), `h.tang@polyu.edu.hk` (H. Tang), `andrew.chan@utas.edu.au` (A. Chan), `Xiaolin.wang@utas.edu.au` (X. Wang).

*Preprint submitted to Elsevier* *26 July 2018*

etc, fluids shows a non-Newtonian manner. Several models and methods have been proposed and applied for different non-Newtonian fluids through porous media. For non-Newtonian fluids through porous media, the difference with the Newtonian fluids is observed in the effective shear stress ($\boldsymbol{\tau}$) and the dynamic viscosities. A large number of models have been proposed in the literature to model all types of non-Newtonian fluids under various flow conditions, e.g. power-law fluids, viscoplastic fluids, viscoelastic fluids, etc [3].

Flow in porous media is usually modeled based on the volume-averaging at the representative elementary volume (REV) scale. In this approach, many models have been introduced in the literature, such as the Darcy, the Darcy-Brinkman, and the Darcy–Brinkman–Forchheimer models. In these models, fluid forces and the solid drag force are considered in the momentum equation [4,5]. In these studies, the continuity, momentum and energy equations of porous media for incompressible Newtonian fluid flows can be summarized as

**Continuity equation:**

$$\nabla \cdot \mathbf{u} = 0 \quad , \tag{1.1}$$

$\mathbf{u}$ is the volume averaged velocity through the expression; $\mathbf{u} = \epsilon\, \mathbf{s}$, where $\mathbf{s} = (s_x, s_y)$ and $\epsilon$ are the fluid velocity and porosity, respectively.

**Momentum equation:**

$$\frac{\rho}{\epsilon}\left[\frac{\partial \mathbf{u}}{\partial t} + (\mathbf{u}\cdot\nabla)\,\mathbf{s}\right] + \frac{1}{\epsilon}\,\nabla(\epsilon\, p) - \frac{\nabla.\boldsymbol{\tau}}{\epsilon} + \mathbf{D} = \mathbf{b} \quad , \tag{1.2}$$

$\rho$, $t$, $p$, and $\mathbf{b}$ are the fluid density, time, pressure, and body forces, e.g. gravity; respectively. $\boldsymbol{\tau}$ is the effective shear stress and for Newtonian fluids were presented as

$$\boldsymbol{\tau} = \eta\, \mathbf{A_1}, \quad \mathbf{A_1} = \nabla\mathbf{u} + (\nabla\mathbf{u})^T \quad , \tag{1.3}$$

where $\eta$ is the effective dynamic viscosity and $\mathbf{A_1}$ is the first Rivlin–Ericksen tensor.

$\mathbf{D}$ is the solid matrix drag per unit volume of the porous medium and was defined as

$$\mathbf{D} = \left[\frac{\mu}{K} + \frac{\rho\, E_\epsilon}{\sqrt{K}}|\mathbf{u}|\right]\mathbf{u}, \quad |\mathbf{u}| = \sqrt{u^2 + v^2}\ , \tag{1.4}$$

$$K = \frac{\epsilon^3\, d^2}{150\,(1-\epsilon)^2}, \quad E_\epsilon = \frac{1.75}{\sqrt{150\,\epsilon^3}} \quad , \tag{1.5}$$

where $\mu$ is the dynamic viscosity and $d$ is the solid particle diameter.

It should be noted the exhibited approach is Darcy–Brinkman–Forchheimer model. But, with removing the shear stress in Eq.(1.2) and the second term in the right side of the Eq.(1.4), Eq.(1.2) satisfies Darcy model. Moreover, with removing the second term in the right side of the Eq.(1.4), Eq.(1.2) desires the Brinkman-extended Darcy model.

**Energy equation:**

$$(\rho\, c_p)_e \frac{\partial T}{\partial t} + (\rho\, c_p)_f\, \mathbf{u}\,.\nabla T = k_e\, \nabla^2 T + \Phi \tag{1.6}$$

where

$$(\rho\, c_p)_e = \epsilon(\rho\, c_p)_f + (1-\epsilon)(\rho\, c_p)_s \tag{1.7}$$

$$k_e = \epsilon k_f + (1-\epsilon) k_s \tag{1.8}$$

Here, $T$, $c_p$, and $k$ are the temperature, heat capacity at constant pressure, and the thermal conductivity, respectively. The subscripts of $f$ and $s$ are the fluid and solid parts.

$\Phi$ is the viscous dissipation and was mentioned as

$$\Phi = \frac{1}{2}\boldsymbol{\tau} : \mathbf{A_1} + \mathbf{D}\cdot\mathbf{u} \tag{1.9}$$

To study the convection process in a porous media, many studies have been applied to the buoyancy-driven flow in a square cavity with vertical sides which are differentially heated as a benchmark problem [6,7]. So, natural convection of porous media in a cavity has been studied by different numerical methods. Here, some important studies in this area have been stated and some other investigations have been referenced. Nithiarasu et al. [8,9] developed a Finite Element Method (FEM) for generalised non-Darcian porous medium model on natural convective flow, taking into account linear and non-linear matrix drag components as well as the inertial and viscous forces within the fluid. A detailed parametric study was presented for natural convective flow inside a rectangular enclosure filled with saturated porous medium of constant or variable porosity. It was observed that the thickness of the porous layer and the nature of variation in porosity significantly affect the natural convective flow pattern as well as the heat transfer features. Guo and Zhao [10] proposed a lattice Boltzmann model for convection heat transfer in porous media. In this model, a new distribution function was introduced to simulate the temperature field in addition to the density distribution function for the velocity field.

The macroscopic equations for convection heat transfer in porous media were recovered from the model through the Chapman-Enskog procedure. Liu et al. [11] developed a two-dimensional (2D) multiple-relaxation-time (MRT) lattice Boltzmann (LB) model for simulating convection heat transfer in porous media at the representative elementary volume scale. In the model, a D2Q9 MRT-LB equation was adopted to simulate the flow field, while a D2Q5 MRT-LB equation was employed to simulate the temperature field. The generalized model was employed to model the momentum transfer, and the effect of the porous media was considered by introducing the porosity into the equilibrium moments, and adding a forcing term to the MRT-LB equation of the flow field in the moment space. Wang et al. [12] developed a modified LBGK model, which incorporates the shear rate and temperature gradient in the equilibrium distribution functions, for incompressible thermal flows in porous media at the representative elementary volume scale. Several benchmark problems were simulated to validate the present model with the local computing scheme for the shear rate and temperature gradient. Das et al. [13] studied the importance of the quadratic (Forchheimer) drag force for the flow through porous media during natural convection within various geometrical shapes (square, rhombus, concave and convex). The numerical simulations were performed via the Galerkin finite element method for various parameters. Two different flow models were considered based on the inclusion of the quadratic drag term (the Forchheimer term); Case 1: the Darcy–Brinkman model and Case 2: the Darcy–Brinkman–Forchheimer model. Das and Basak [14] followed their previous study for discretely heated porous square and triangular enclosures during natural convection. Five different discrete heating strategies were considered and heatline method was implemented to visualize the heat flow pattern within the cavities for a wide range of parameters.

Lattice Boltzmann method (LBM) has been demonstrated to be a very effective mesoscopic numerical method to model a broad variety of complex fluid flow phenomena. This is because the main equation of the LBM is hyperbolic and can be solved locally, explicitly, and efficiently on parallel computers. However, the specific relation between the relaxation time and the viscosity has caused LBM not to have the considerable success in non-Newtonian fluid especially on energy equations. In this connection, Fu et al. [15] proposed a new equation for the equilibrium distribution function, modifying the LB model. Here, this equilibrium distribution function is altered in different directions and nodes while the relaxation time is fixed. Independency of the method to the relaxation time in contrast with common LBM provokes the method to solve different non-Newtonian fluid energy equations successfully as the method protects the positive points of LBM simultaneously. In addition, the validation of the method and its mesh independency demonstrates that it is more capable than conventional LBM. Huilgol and Kefayati [1] explained and derived the two and three dimensional equations of continuum mechanics for this method and demonstrated that the theoretical development can be applied to all fluids, whether they be Newtonian, or power law fluids, or viscoelastic and viscoplastic fluids. Following the previous study, Huilgol and Kefayati [2] derived the two and three dimensional equations of this method for the cylindrical and spherical coordinates. Validation results obtained through the modelling of a mixed convection flow of a Bingham fluid in a lid-driven square cavity, and the steady flow of a Bingham fluid in a pipe of square cross-section. Next, using the cylindrical coordinate version of the evolution equations, numerical modelling of the steady flow of a Bingham fluid and the Herschel–Bulkley fluid in a pipe of circular cross-section were performed and compared with the simulation results using the augmented Lagrangian method as well as the analytical solutions for the velocity field and the flow rate.

The main aim of this study is to introduce a new thermal Lattice Boltzmann method for non-Newtonian fluid flows through porous media. In section 2, following recent studies by Huilgol and Kefayati [1,2], we propose a general LBM for non-Newtonian fluids through porous media. This proposed LBM cover all parameters in the momentum and energy equations; including force terms, energy sources, and viscous dissipation. In this method, we apply the non-dimensional equations of continuum mechanics in the proposed LBM equations. In section 3, the dimensional equations of natural convection in a porous cavity, using Darcy–Brinkman–Forchheimer model are mentioned and these equations are non-dimensionalized by a new method; which the effect of porosity is just observed in non-dimensional parameters instead of the main momentum and energy equations. Next, the non-dimensional equations were applied to the proposed LBM while the employed algorithm is explained. The obtained results of natural convection within a porous cavity and enclosures filled with power-law and Bingham non-Newtonian fluids were compared with previous studies in the forms of isotherms, streamlines, and the average Nusselt number. Finally, results of natural convection in a porous enclosure filled with power-law and Bingham fluids is studied and results of the heat transfer and the fluid flow are presented.

## 2 Mathematical model

### *2.1 Background*

Initially, the Lattice Boltzmann Equation (LBE) models were generated from lattice gas (LG) automata [16–18]. The lattice gas automaton is constructed as a simplified, fictitious molecular dynamic in which space, time, and particle velocities are all discrete [19]. From this perspective, the lattice gas method is often called lattice gas cellular automata.

let $f = f(\mathbf{x}, \boldsymbol{\xi}, t)$ be the probability of finding a particle with the velocity $\boldsymbol{\xi}$ near the point $\mathbf{x}$ at time $t$. The Boltzmann equation for this distribution function, in the absence of external forces, is given by

$$\frac{\partial f}{\partial t} + \nabla f \cdot \boldsymbol{\xi} + \frac{1}{\lambda} f = N(f), \tag{2.1}$$

where $\boldsymbol{\xi}$ is the microscopic velocity, $\lambda$ is the relaxation time due to collision and $N(f)$ is a measure of the net number of molecules which disappear from the region due to inter-molecular collisions.
The macroscopic variables are the density of mass $\rho$, the velocity field $\mathbf{u}$ and the absolute temperature $T$. These are related to the distribution function $f$ through the following integrals in momentum space:

$$\rho = \int f \, d\boldsymbol{\xi}, \quad \rho \mathbf{u} = \int \boldsymbol{\xi} f \, d\boldsymbol{\xi}, \quad \rho \varsigma = \frac{1}{2} \int |\boldsymbol{\xi} - \mathbf{u}|^2 f \, d\boldsymbol{\xi}, \tag{2.2}$$

where $\varsigma = D_0 RT/2$, with $D_0$ being the number of degrees of freedom of a particle and $R$ is the ideal gas constant. Note that we have used $d\boldsymbol{\xi} = d\xi_1 \cdots d\xi_D$, where $D \in [2, 3]$ stands for the dimension of the physical space.

A particular simple linearized version of the collision operator makes use of a relaxation time towards the local equilibrium using a single time relaxation. The relaxation term is known as the Bhatnagar-Gross-Krook (BGK) collision operator (Bhatnagar et al [20]) and has been independently suggested [21,22]. In the BGK approximation, the collision operator is assumed to be given by $N(f) = h(\mathbf{x}, \boldsymbol{\xi}, t)/\lambda$, where the collision function $h(\mathbf{x}, \boldsymbol{\xi}, t)$ has the form:

$$h(\mathbf{x}, \boldsymbol{\xi}, t) = \frac{\rho}{(2\pi RT)^{D/2}} \exp\left[ -\frac{|\boldsymbol{\xi} - \mathbf{u}|^2}{2RT} \right] \tag{2.3}$$

integrating (2.1) over a small time interval, we have

$$f(\mathbf{x} + \boldsymbol{\xi} \triangle t, \boldsymbol{\xi}, t + \triangle t) - f(\mathbf{x}, \boldsymbol{\xi}, t) = -\frac{1}{\phi} [f(\mathbf{x}, \boldsymbol{\xi}, t) - h(\mathbf{x}, \boldsymbol{\xi}, t)], \tag{2.4}$$

where $\phi = \lambda / \triangle t$ is the non-dimensional relaxation time. For dimension and the number of nodes, the parameter of DmQn is introduced where m is the dimension of the study (2D or 3D) and n is the number of nodes in the selected lattice.

In the D2Q9 model, there are nine discrete velocities (Fig.1): $\{\boldsymbol{\xi}_\alpha, \ \alpha = 0, 1, \cdots, 8\}$. The configuration space is discretised into a square lattice with a lattice constant $\triangle x = \sqrt{3RT} \ \triangle t$. In fact, in an isothermal problem, the temperature $T$ has no physical significance and thus, one can choose $\triangle x$ as a fundamental quantity instead, leading to $\sqrt{3RT} = c = \triangle x / \triangle t$, where the lattice speed $c$ is related to the speed of sound $c_s$ through $c^2 = 3c_s^2$. Thus,

$RT = c_s^2 = c^2/3$. The nine lattice points are located at the centre of the lattice, at the four midpoints of the edges of the square and at the four vertices. One identifies $\alpha_0 = (0,0)$ as the centre of the lattice, $\{\alpha_1, \alpha_3, \alpha_5, \alpha_7\}$ as the midpoints of the four sides: $(\pm 1, 0), (0, \pm 1)$, and $\{\alpha_2, \alpha_4, \alpha_6 \alpha_8\} = (\pm 1, \pm 1)$ as the vertices. The lattice velocity vector is given by $\boldsymbol{\xi}_0 = \mathbf{0}$. Next, the velocities for $\alpha = 1, 3, 5, 7$, have the form $c(\pm 1, 0), c(0, \pm 1)$, and for $\alpha = 2, 4, 6, 8$, they have the form $c(\pm 1, \pm 1)$.

The equilibrium distribution function for the D2Q9 model is given by

$$h_\alpha = w_\alpha \, \rho \left[ 1 + \frac{3(\boldsymbol{\xi}_\alpha \cdot \mathbf{u})}{c^2} + \frac{9(\boldsymbol{\xi}_\alpha \cdot \mathbf{u})^2}{c^4} - \frac{3|\mathbf{u}|^2}{2c^2} \right], \tag{2.5}$$

where

$$w_\alpha = \begin{cases} 4/9, & \alpha = 0, \\ 1/9, & \alpha = 1, 3, 5, 7, \\ 1/36, & \alpha = 2, 4, 6, 8. \end{cases} \tag{2.6}$$

with

$$\boldsymbol{\xi}_\alpha = \begin{cases} (0,0), & \alpha = 0, \\ c(\cos\theta_\alpha, \sin\theta_\alpha) & \alpha = 1, 3, 5, 7, \\ c\sqrt{2}(\cos\theta_\alpha, \sin\theta_\alpha), & \alpha = 2, 4, 6, 8. \end{cases} \tag{2.7}$$

In this approach, the pressure $p = \rho c_s^2$ has a thermodynamic form only, with $c_s$ being the speed of sound. The expression for the kinematic viscosity is given by $\nu = (2\tau - 1) c^2 \triangle t / 6$, and depends on the non-dimensional relaxation time $\tau$ and the time step $\triangle t$.

### *2.2 The applied model*

With the assumption that the collision term in Eq. (2.1) is written by $N(f) = f^{eq}/\lambda$, it would be as follows:

$$\frac{\partial f_\alpha}{\partial t} + \boldsymbol{\xi}_\alpha \cdot \nabla_{\mathbf{x}} f_\alpha - F_\alpha = -\frac{1}{\beta \, \phi} (f_\alpha - f_\alpha^{eq}), \tag{2.8}$$

where $\beta$ is a small parameter to be prescribed when numerical simulations are considered. $\phi$ is the relaxation time. The parameter of $F_\alpha$ is the force term.

To proceed, one assumes that $f_\alpha$ has the following expansion:

$$f_\alpha = f_\alpha^{eq} + \beta f_\alpha^{(1)} + \beta^2 f_\alpha^{(2)} + O(\beta^3). \tag{2.9}$$

The novelty of the approach by Fu and So [15] lies in expanding the equilibrium lattice function $f_\alpha^{eq}$ as a quadratic in the particle velocity $\boldsymbol{\xi}_\alpha$. The main reason for the selection of the expansions are to recover all parameters in the momentum equations properly. The accuracy of the introduced parameters can be observed in the Appendix A.

$$f_\alpha^{eq} = A_\alpha + \boldsymbol{\xi}_\alpha \cdot \mathbf{B}_\alpha + (\boldsymbol{\xi}_\alpha \otimes \boldsymbol{\xi}_\alpha) : \mathbf{C}_\alpha, \tag{2.10}$$

where $\mathbf{B}_\alpha$ is a vector and $\mathbf{C}_\alpha$ is a $2 \times 2$ symmetric matrix. The following relations must hold:

$$\sum_{\alpha=0}^{8} f_\alpha^{eq} = \rho, \tag{2.11}$$

$$\sum_{\alpha=0}^{8} f_\alpha^{eq} \boldsymbol{\xi}_\alpha = \rho \mathbf{u}, \quad \mathbf{u} = u\mathbf{i} + v\mathbf{j}, \tag{2.12}$$

$$\sum_{\alpha=0}^{8} f_\alpha^{eq} \boldsymbol{\xi}_\alpha \otimes \boldsymbol{\xi}_\alpha = \mathbf{M}, \tag{2.13}$$

$$\sum_{\alpha=0}^{8} f_\alpha^{(n)} = 0, \quad n \geq 1, \tag{2.14}$$

$$\sum_{\alpha=0}^{8} f_\alpha^{(n)} \boldsymbol{\xi}_\alpha = 0, \quad n \geq 1. \tag{2.15}$$

where

$$\mathbf{M} = \frac{\mathbf{1}}{\epsilon} \begin{bmatrix} \rho u s_x + \epsilon p - \tau_{xx} & \rho u s_y - \tau_{xy} \\ \rho v s_x - \tau_{xy} & \rho v s_y + \epsilon p - \tau_{yy} \end{bmatrix}. \tag{2.16}$$

we have $\mathbf{u} = \epsilon \mathbf{s}$, so $\mathbf{M}$ changes to

$$\mathbf{M} = \frac{\mathbf{1}}{\epsilon} \begin{bmatrix} \rho \frac{u^2}{\epsilon} + \epsilon p - \tau_{xx} & \rho \frac{uv}{\epsilon} - \tau_{xy} \\ \rho \frac{uv}{\epsilon} - \tau_{xy} & \rho \frac{v^2}{\epsilon} + \epsilon p - \tau_{yy} \end{bmatrix}. \tag{2.17}$$

In the above set, $\tau_{xx}, \tau_{xy} = \tau_{yx}, \tau_{yy}$ are the effective stresses which can be defined through any relevant constitutive relation.

The relation between the above parameters and non-dimensional macroscopic values are as follows

$$A_0 = \rho - \frac{2p}{\sigma^2} - \frac{\rho |\mathbf{u}/\epsilon|^2}{\sigma^2}, \quad A_\alpha = 0, \; \alpha = 1, 2, \cdots, 8. \tag{2.18}$$

$$\mathbf{B}_1 = \frac{\rho \mathbf{u}}{2\sigma^2} = \mathbf{B}_\alpha,\ \alpha = 1,3,5,7; \quad \mathbf{B}_\alpha = \mathbf{0},\ \alpha = 0,2,4,6,8. \tag{2.19}$$

Next, the matrices $\mathbf{C}_\alpha$ are such that $\mathbf{C}_0 = 0;\ \mathbf{C}_1 = \mathbf{C}_\alpha,\ \alpha = 1,3,5,7;\ \mathbf{C}_2 = \mathbf{C}_\alpha,\ \alpha = 2,4,6,8$, where

$$\mathbf{C}_1 = \begin{bmatrix} C_{11} & 0 \\ 0 & C_{22} \end{bmatrix}, \quad C_{11} = \frac{1}{2\sigma^4}\left(p + \rho\,(\frac{u}{\epsilon})^2 - \frac{\tau_{xx}}{\epsilon}\right), \tag{2.20a}$$

$$C_{22} = \frac{1}{2\sigma^4}\left(p + \rho\,(\frac{v}{\epsilon})^2 - \frac{\tau_{yy}}{\epsilon}\right), \tag{2.20b}$$

$$\mathbf{C}_2 = \begin{bmatrix} 0 & C_{12} \\ C_{21} & 0 \end{bmatrix}, \quad C_{12} = C_{21} = \frac{1}{8\sigma^4}\left(\rho(\frac{uv}{\epsilon^2}) - \frac{\tau_{xy}}{\epsilon}\right). \tag{2.21}$$

The constant $\sigma$ has to be chosen with care for it affects numerical stability; its choice depends on the problem. The method for finding the parameter $\sigma$ which satisfies the Courant-Friedrichs-Lewy (CFL) condition is described in Appendix B.

The body force term $F_\alpha$ can be defined as

$$F_\alpha = 0, \quad \alpha = 0,2,4,6,8, \tag{2.22a}$$

$$F_\alpha = \frac{1}{2\sigma^2}\mathbf{f} \cdot \boldsymbol{\xi}_\alpha, \quad \alpha = 1,3,5,7 \tag{2.22b}$$

where $\mathbf{f}$ represents the total body force due to the presence of a porous medium $\mathbf{D}$ and other external force fields $\mathbf{b}$ as

$$\mathbf{f} = \mathbf{b} - \mathbf{D} \tag{2.23}$$

In order to obtain the energy equation, an internal energy distribution function $g_\alpha$ is introduced and it is assumed to satisfy an evolution equation similar to that for $f_\alpha$. Thus,

$$\frac{\partial g_\alpha}{\partial t} + \boldsymbol{\xi}_\alpha \cdot \nabla_{\mathbf{x}} g_\alpha - G_\alpha = -\frac{1}{\beta\phi}(g_\alpha - g_\alpha^{eq}). \tag{2.24}$$

Here, $g_\alpha^{eq}$ has a linear form in the lattice velocity vector. The main reason for the selection of the expansions are to recover all parameters in the energy equations properly. The accuracy of the introduced parameters can be observed in the Appendix C.

$$g_\alpha^{eq} = D_\alpha + \boldsymbol{\xi}_\alpha \cdot \mathbf{E}_\alpha. \tag{2.25}$$

And,

$$g_\alpha = g_\alpha^{eq} + \beta g_\alpha^{(1)} + \beta^2 g_\alpha^{(2)} + O(\beta^3), \tag{2.26}$$

with the requirement that

$$\sum_{\alpha=0}^{8} g_\alpha^{(n)} = 0, \quad n \geq 1. \tag{2.27}$$

The energy equation applicable to an incompressible porous media on the volume averaging at REV can be presented by

$$\rho \frac{de}{dt} = \frac{1}{2} \boldsymbol{\tau} : \mathbf{A_1} - \nabla \cdot \mathbf{q} + \rho r, \tag{2.28}$$

where $e$ is the effective internal energy, $\mathbf{q}$ is the effective heat efflux vector and $r$ is the external supply.

Next, the following consistency relations must hold:

$$\sum_{\alpha=0}^{8} g_\alpha^{eq} = \rho e + \frac{1}{2}\rho |\mathbf{s}\,\mathbf{u}|, \tag{2.29}$$

$$\sum_{\alpha=0}^{8} g_\alpha^{eq} \boldsymbol{\xi}_\alpha = \left(\epsilon\, p + \rho e + \frac{1}{2}\rho |\mathbf{s}\,\mathbf{u}|\right)\mathbf{s} - \boldsymbol{\tau}\mathbf{s} + \mathbf{q}, \tag{2.30}$$

$$\sum_{\alpha=0}^{8} G_\alpha = \mathbf{f} \cdot \mathbf{u} - \rho r. \tag{2.31}$$

One way of satisfying the above is to assume, as before, that the scalars $D_\alpha$ are such that $D_\alpha = D_1,\ \alpha = 1, 3, 5, 7$, and $D_\alpha = D_2,\ \alpha = 2, 4, 6, 8$, and set

$$D_0 = \rho e + \frac{1}{2}\rho |\mathbf{s}\,\mathbf{u}|, \quad D_1 = 0, \quad D_2 = 0. \tag{2.32}$$

In addition, it is assumed that the vectors $\mathbf{E}_\alpha$ are defined through $\mathbf{E}_0 = \mathbf{0},\ \mathbf{E}_\alpha = \mathbf{E}_1,\ \alpha = 1, 3, 5, 7; \mathbf{E}_\alpha = \mathbf{E}_2,\ \alpha = 2, 4, 6, 8$, where

$$\mathbf{E}_1 = \frac{1}{2\sigma^2}\left(\epsilon\, p + \rho\, e + \frac{1}{2}\rho |\mathbf{s}\,\mathbf{u}|\right)\mathbf{s} - \boldsymbol{\tau}\mathbf{s} + \mathbf{q}, \quad \mathbf{E}_2 = \mathbf{0}. \tag{2.33}$$

Finally, the scalars $G_\alpha$ must satisfy

$$G_\alpha = \frac{1}{2}\mathbf{f} - \frac{1}{4}\rho r, \quad \alpha = 1, 3, 5, 7, \tag{2.34}$$

$$G_\alpha = 0,\ \alpha = 0, 2, 4, 6, 8. \tag{2.35}$$

## 3 Validation and Results

To validate the present model, we applied it to natural convection of Newtonian fluids in a porous cavity, using the Darcy–Brinkman–Forchheimer model (Fig.2). Based on the above assumptions, and applying the Boussinesq approximation, the mass, momentum, and energy equations are [8,9]:

$$\frac{\partial u}{\partial x} + \frac{\partial v}{\partial y} = 0, \tag{3.1}$$

$$\frac{\rho}{\epsilon}\left(\frac{\partial u}{\partial t} + u\frac{\partial s_x}{\partial x} + v\frac{\partial s_x}{\partial y}\right) = -\frac{1}{\epsilon}\frac{\partial\,(\epsilon\, p)}{\partial x} + \frac{1}{\epsilon}\left(\frac{\partial \tau_{xx}}{\partial x} + \frac{\partial \tau_{xy}}{\partial y}\right) - D_x, \tag{3.2}$$

$$\frac{\rho}{\epsilon}\left(\frac{\partial v}{\partial t} + u\frac{\partial s_y}{\partial x} + v\frac{\partial s_y}{\partial y}\right) = -\frac{1}{\epsilon}\frac{\partial\,(\epsilon\, p)}{\partial y} + \frac{1}{\epsilon}\left(\frac{\partial \tau_{yy}}{\partial y} + \frac{\partial \tau_{xy}}{\partial x}\right) + g\rho\beta_T(T - T_C) - D_y, \tag{3.3}$$

In the above equations, ($\mathbf{x} = x\,\mathbf{i} + y\,\mathbf{j}$), $t$, $\boldsymbol{\tau}$ are the Cartesian coordinates, time, and shear stress; respectively. In addition, ($\mathbf{u} = u\,\mathbf{i} + v\,\mathbf{j}$), $T$, and $g$ are the dimensional velocities, temperature, and gravity acceleration; respectively. $\beta_T$ is the coefficient of thermal expansion and $\rho$ is density. $\mathbf{D} = (D_x, D_y)$ is the solid matrix drag per unit volume of the porous medium and is expressed in Eq.(1.4).

$$(\rho\, c_p)_e\frac{\partial T}{\partial t} + (\rho\, c_p)_f\, u\frac{\partial T}{\partial x} + (\rho\, c_p)_f\, v\frac{\partial T}{\partial y} = k_e\left(\frac{\partial^2 T}{\partial x^2} + \frac{\partial^2 T}{\partial y^2}\right) \tag{3.4}$$

where

$$(\rho\, c_p)_e = \epsilon(\rho\, c_p)_f + (1-\epsilon)(\rho\, c_p)_s \qquad k_e = \epsilon k_f + (1-\epsilon)k_s \tag{3.5}$$

$$\Lambda = \frac{(\rho\, c_p)_e}{(\rho\, c_p)_f} \tag{3.6}$$

Many studies with different numerical methods have been conducted; by researchers, in to this problem [8–14]. In these studies, the parameter $\frac{(\rho\, c_p)_e}{(\rho\, c_p)_f}$ in the energy equation and the viscosity ratio $J = \frac{\eta}{\mu}$ are equal to one. In addition, the viscous dissipation is negligible. So, in the present study similar to the cited investigations, we assume that the thermal properties of the solid matrix and the fluid have been taken to be identical ($\Lambda = 1, k_e = k_s = k_f$), so the energy equation is simplified as

$$\frac{\partial T}{\partial t} + u\frac{\partial T}{\partial x} + v\frac{\partial T}{\partial y} = \alpha\left(\frac{\partial^2 T}{\partial x^2} + \frac{\partial^2 T}{\partial y^2}\right) \tag{3.7}$$

$\alpha = \frac{k_e}{\rho c_{p_f}}$, $k_e$, and $c_{p_f}$ are the thermal diffusivity, the effective thermal conductivity, and the specific heat at constant pressure, respectively.

Here, we have applied a recent method by Das et al. [13,14] to obtain the non-dimensional equations which are independent to the porosity and the porosity effect is employed to non-dimensional parameters. So, in this method, we can study the effect of porosity, using the non-dimensional equations and therefore this approach improves the stability in the applied method. We define the buoyancy velocity scale $U = \left(\frac{\alpha_e}{L}\right) {Ra_m}^{0.5}$ as $Ra_m$ is the modified Rayleigh number. In order to proceed to the numerical solution of the system, the following non dimensional variables are introduced where

$$t^* = \frac{t\,U}{L}, \quad x^* = \frac{\mathbf{x}}{L}, \quad \mathbf{u}^* = \frac{\mathbf{u}}{U}, \tag{3.8}$$

$$T^* = (T - T_C)/\Delta T, \quad \Delta T = T_H - T_C, \quad p^* = \frac{p}{\rho\,U^2} \tag{3.9}$$

$$\alpha_e = \frac{k_e}{\epsilon\,\rho\,cp_f}\,, \quad Ra_m = \frac{\rho^2\,\beta_T\,gL^3\Delta T\,Pr_m}{\eta^2}, \tag{3.10}$$

$$Pr_m = \frac{\eta}{\alpha_e\,\rho}\,, \quad Da_m = \frac{k}{\epsilon\,L^2}\,. \tag{3.11}$$

In other words, the relationship between the modified and actual Prandtl, Rayleigh and Darcy numbers are $Pr_m = Pr \times \epsilon$, $Ra_m = Ra \times \epsilon$, and $Da_m = Da/\epsilon$.

By substitution of Eqs. (3.8) - (3.11) in the dimensional equations and dropping the asterisks, the following system of non-dimensional mass, momentum, and energy equations are derived

$$\frac{\partial u}{\partial x} + \frac{\partial v}{\partial y} = 0 \quad , \tag{3.12}$$

$$\begin{aligned}\frac{\partial u}{\partial t}+u\frac{\partial u}{\partial x}+v\frac{\partial u}{\partial y}=-\frac{\partial p}{\partial x}+\frac{Pr_m}{\sqrt{Ra_m}}\left(\frac{\partial \tau_{xx}}{\partial x}+\frac{\partial \tau_{xy}}{\partial y}\right)\\ -\frac{Pr_m\ u}{Da_m\sqrt{Ra_m}}-\frac{u\left|\mathbf{u}\right|}{\sqrt{Da_m}}\frac{1.75}{\sqrt{150}}\end{aligned} \tag{3.13}$$

$$\begin{aligned}\frac{\partial v}{\partial t}+u\frac{\partial v}{\partial x}+v\frac{\partial v}{\partial y}=-\frac{\partial p}{\partial y}+\frac{Pr_m}{\sqrt{\mathrm{Ra}}}\left(\frac{\partial \tau_{yx}}{\partial x}+\frac{\partial \tau_{yy}}{\partial y}\right)+Pr_m T\\ -\frac{Pr_m\ v}{Da_m\sqrt{Ra_m}}-\frac{v\left|\mathbf{u}\right|}{\sqrt{Da_m}}\frac{1.75}{\sqrt{150}}\end{aligned} \tag{3.14}$$

$$\frac{\partial T}{\partial t}+u\frac{\partial T}{\partial x}+v\frac{\partial T}{\partial y}=\frac{1}{\sqrt{Ra_m}}\left(\frac{\partial^2 T}{\partial x^2}+\frac{\partial^2 T}{\partial y^2}\right) \tag{3.15}$$

Based on the non-dimensional equations, the porosity in Eqs.(2.19)–(2.22) are vanished while affect the applied force term. So, the relation between the above non-dimensional macroscopic values and variables of the equilibrium lattice function (eq.(2.10)) are as follows:

$$A_0=\rho-\frac{2p}{\sigma^2}-\frac{\rho|\mathbf{u}|^2}{\sigma^2},\quad A_\alpha=0,\ \alpha=1,2,\cdots,8. \tag{3.16}$$

$$\mathbf{B}_1=\frac{\rho\mathbf{u}}{2\sigma^2}=\mathbf{B}_\alpha,\ \alpha=1,3,5,7;\quad \mathbf{B}_\alpha=\mathbf{0},\ \alpha=0,2,4,6,8. \tag{3.17}$$

$$\mathbf{C}_1=\begin{bmatrix}C_{11} & 0\\ 0 & C_{22}\end{bmatrix},\quad C_{11}=\frac{1}{2\sigma^4}\left(p+\rho u^2-\frac{Pr_m}{\sqrt{Ra_m}}\tau_{xx}\right),\quad C_{22}=\frac{1}{2\sigma^4}\left(p+\rho v^2-\frac{Pr_m}{\sqrt{Ra_m}}\tau_{yy}\right), \tag{3.18}$$

$$\mathbf{C}_2=\begin{bmatrix}0 & C_{12}\\ C_{21} & 0\end{bmatrix},\quad C_{12}=C_{21}=\frac{1}{8\sigma^4}\left(\rho uv-\frac{Pr_m}{\sqrt{Ra_m}}\tau_{xy}\right). \tag{3.19}$$

The body force term $F_\alpha$ in Eqs.(2.23)–(2.24) can be defined as

$$F_\alpha=0,\quad \alpha=0,2,4,6,8, \tag{3.20a}$$

$$F_\alpha=\frac{1}{2\sigma^2}\mathbf{f}\cdot\boldsymbol{\xi}_\alpha,\quad \alpha=1,3,5,7 \tag{3.20b}$$

$$\begin{aligned}\mathbf{f} = &\left[-\frac{Pr_m\ u}{Da_m\sqrt{Ra_m}} - \frac{u\,|\mathbf{u}|}{\sqrt{Da_m}}\frac{1.75}{\sqrt{150}}\right]\mathbf{i} \\ &+\left[Pr_m T - \frac{Pr_m\ v}{Da_m\sqrt{Ra_m}} - \frac{v\,|\mathbf{u}|}{\sqrt{Da_m}}\frac{1.75}{\sqrt{150}}\right]\mathbf{j}\end{aligned} \tag{3.21}$$

The main equations of the discrete particle distribution function (2.8) is solved by the splitting method of Toro [23]. Hence, the equations can be separated into two parts. The first one is the streaming section which is written as

$$\frac{\partial f_\alpha}{\partial t} + \boldsymbol{\xi}_\alpha \cdot \nabla_{\mathbf{x}} f_\alpha - F_\alpha = 0. \tag{3.22}$$

It should be noted that the splitting method is only first-order accurate in time. Since $\beta = \Delta t$ has been chosen, it is consistent with the asymptotic expansion error, which is given by $\mathrm{O}(\beta) = \mathrm{O}(\Delta \mathrm{t})$.

Eqs.(3.22) has been solved with the method of Lax and Wendroff [24] and the following equations are used.

$$\begin{aligned} f_\alpha^{n+1}(i,j) = f_\alpha^n(i,j) &- \frac{\Delta t}{2\Delta x}\xi_\alpha(i)\left[f_\alpha^n(i+1,j) - f_\alpha^n(i-1,j)\right] \\ &- \frac{\Delta t}{2\Delta y}\xi_\alpha(j)\left[f_\alpha^n(i,j+1) - f_\alpha^n(i,j-1)\right] + \\ &\frac{\Delta t^2}{2\Delta x^2}{\xi_\alpha}^2(i)\left[f_\alpha^n(i+1,j) - 2f_\alpha^n(i,j) + f_\alpha^n(i-1,j)\right] + F_\alpha(i)\Delta t + \\ &\frac{\Delta t^2}{2\Delta y^2}{\xi_\alpha}^2(j)\left[f_\alpha^n(i,j+1) - 2f_\alpha^n(i,j) + f_\alpha^n(i,j-1)\right] + F_\alpha(j)\Delta t\ ,\end{aligned} \tag{3.23}$$

In Eqs.(3.23), we have put

$$\xi_\alpha(i) = \boldsymbol{\xi}_\alpha \cdot \mathbf{i}, \quad \xi_\alpha(j) = \boldsymbol{\xi}_\alpha \cdot \mathbf{j}, \quad F_\alpha(i) = \mathbf{F}_\alpha \cdot \mathbf{i}, \quad F_\alpha(j) = \mathbf{F}_\alpha \cdot \mathbf{j}. \tag{3.24}$$

The second part is the collision section which is as follows:

$$\frac{\partial f_\alpha}{\partial t} = -\frac{1}{\beta\phi}(f_\alpha(\mathbf{x},t) - f_\alpha^{eq}(\mathbf{x},t)), \tag{3.25}$$

Eqs.(3.25) can be solved by using the Euler method and the choice of $\lambda\phi$ is taken as the time step ($\Delta t$). That is

$$\frac{f_\alpha(\mathbf{x}, t+\Delta t) - f_\alpha(\mathbf{x}, t)}{\Delta t} = -\frac{1}{\beta\phi}(f_\alpha(\mathbf{x}, t) - f_\alpha^{eq}(\mathbf{x}, t)), \tag{3.26}$$

from which one obtains

$$f_\alpha(\mathbf{x}, t+\Delta t) = f_\alpha^{eq}(\mathbf{x}, t), \tag{3.27}$$

In the energy equation section, the parameters in Eqs. (2.33)–(2.36) are obtained as

$$D_0 = T, \quad D_1 = 0, \quad D_2 = 0. \tag{3.28}$$

$$\mathbf{E}_1 = \frac{1}{2\,\sigma^2}\left(\mathbf{u}\,T - \frac{1}{\sqrt{Ra_m}}\,\frac{\partial T}{\partial \mathbf{x}}\right) \quad \mathbf{E}_2 = 0\,, \tag{3.29}$$

and $G_\alpha = 0$.

The main equations of the internal energy distribution function are solved by the splitting method of Toro [23]. Hence, the equations can be separated into two parts. The first one is the streaming section which is written as

$$\frac{\partial g_\alpha}{\partial t} + \boldsymbol{\xi}_\alpha \cdot \nabla_{\mathbf{x}} g_\alpha = 0. \tag{3.30}$$

Eqs.(3.30) have been solved with the method of Lax and Wendroff [24] and the following equations are used.

$$\begin{aligned} g_\alpha^{n+1}(i,j) = g_\alpha^n(i,j) - \frac{\Delta t}{2\Delta x}\xi_\alpha(i)\left[g_\alpha^n(i+1,j) - g_\alpha^n(i-1,j)\right] \\ - \frac{\Delta t}{2\Delta y}\xi_\alpha(j)\left[g_\alpha^n(i,j+1) - g_\alpha^n(i,j-1)\right] + \\ \frac{\Delta t^2}{2\Delta x^2}{\xi_\alpha}^2(i)\left[g_\alpha^n(i+1,j) - 2g_\alpha^n(i,j) + g_\alpha^n(i-1,j)\right] + \\ \frac{\Delta t^2}{2\Delta y^2}{\xi_\alpha}^2(j)\left[g_\alpha^n(i,j+1) - 2g_\alpha^n(i,j) + g_\alpha^n(i,j-1)\right] \end{aligned} \tag{3.31}$$

The second part is the collision section which is as follows:

$$\frac{\partial g_\alpha}{\partial t} = -\frac{1}{\beta\phi}(g_\alpha(\mathbf{x}, t) - g_\alpha^{eq}(\mathbf{x}, t)). \tag{3.32}$$

Eqs.(3.32) can be solved by using the Euler method and the choice of $\lambda\phi$ is taken as the time step ($\Delta t$). That is

$$\frac{g_\alpha(\mathbf{x}, t+\Delta t) - g_\alpha(\mathbf{x}, t)}{\Delta t} = -\frac{1}{\beta\phi}(g_\alpha(\mathbf{x}, t) - g_\alpha^{eq}(\mathbf{x}, t)), \tag{3.33}$$

from which one obtains

$$g_\alpha(\mathbf{x}, t+\Delta t) = g_\alpha^{eq}(\mathbf{x}, t). \tag{3.34}$$

For a Newtonian fluid case, the non-dimensional effective stresses are as

$$\tau_{xx} = 2\,\frac{\partial u}{\partial x}\,, \quad \tau_{yy} = 2\,\frac{\partial v}{\partial y}\,, \quad \tau_{xy} = \tau_{yx} = \frac{\partial u}{\partial y} + \frac{\partial v}{\partial x} \tag{3.35}$$

An extensive mesh testing procedure was conducted to guarantee a grid independent solution. Six different mesh combinations were explored for the case of $Ra = 10^5$, $Da = 10^{-2}$, $\epsilon = 0.4$, and $Pr = 1$. The average Nusselt numbers on the hot wall have been studied. It was confirmed that the grid size (150×150) ensures a grid independent solution as portrayed by Table 1. In addition, we set the time step $\Delta t = 0.001$ for this calculation and based on the validations, the final (developed) stage was defined at the non-dimensional time $t^* = 200$. The applied code for the fluid flow and heat transfer is validated by the study of Liu et al. [11] in the Figs.3 and 4. In addition, to have more precise comparison, we investigated the average Nusselt number on the hot wall with previous studies of Nithiarasu et al. [8], Guo and Zhao [10], Liu et al. [11] and Wang et al.[12] in the Table.2 in different Rayleigh and Darcy numbers at $Pr = 1$. The local and average Nusselt numbers on the hot wall are calculated as

$$\mathrm{Nu} = -\left(\frac{\partial T}{\partial x}\right)\Bigg|_{x=0}, \tag{3.36}$$

$$\mathrm{Nu}_{\mathrm{avg}} = \int_0^1 \mathrm{Nu}\, dy. \tag{3.37}$$

To check the accuracy of the present results for power-law fluid, the present code is validated by a normalized average Nusselt number (The normalized average Nusselt number expresses Nusselt number at any power-law indexes to the Newtonian fluid which is written $(\frac{\mathrm{Nu}_{\mathrm{avg}}(n)}{\mathrm{Nu}_{\mathrm{avg}}(n=1)})$) with published studies on natural convection of non-Newtonian power-law fluids in a cavity [25,26]. The results are compared in Table 3 as they have a good agreement between the compared studies.

In this section, we study natural convection in a porous cavity filled with power-law fluids flows. The applied equation in this part is similar to Eqs. (3.14)–(3.36) and the differences are the non-dimensional effective stress tensor and the effective dynamic viscosity as well as the fluid viscosity. It should be noted that it is assumed, similar to the studied Newtonian fluid case, the dynamic viscosity ratio (J) is equal to one. For power-law fluids, the non-dimensional effective stress tensor, the effective dynamic viscosity ($\eta\,(\dot{\gamma})$) are as

$$\boldsymbol{\tau} = \eta\,(\dot{\gamma})\,\mathbf{A_1}\,, \qquad \eta\,(\dot{\gamma}) = \dot{\gamma}^{(n-1)} \tag{3.38}$$

$n$ is the power-law index and $\dot{\gamma}$ is the shear rate

$$\dot{\gamma} = \frac{1}{\sqrt{2}}\sqrt{\mathbf{A_1} : \mathbf{A_1}} \tag{3.39}$$

so, for the studied two-dimensional case, the shear rate is as

$$\dot{\gamma} = \left\{ 2\left[ \left(\frac{\partial u}{\partial x}\right)^2 + \left(\frac{\partial v}{\partial y}\right)^2 \right] + \left(\frac{\partial v}{\partial x} + \frac{\partial u}{\partial y}\right)^2 \right\}^{\frac{1}{2}} \tag{3.40}$$

Finally, for a power-law fluid case, the non-dimensional effective stresses are as

$$\tau_{xx} = 2\,\eta(\dot{\gamma})\,\frac{\partial u}{\partial x}\,, \qquad \tau_{yy} = 2\,\eta(\dot{\gamma})\,\frac{\partial v}{\partial y}\,, \qquad \tau_{xy} = \tau_{yx} = \eta(\dot{\gamma})\,\left(\frac{\partial u}{\partial y} + \frac{\partial v}{\partial x}\right) \tag{3.41}$$

Fig.5 demonstrates the isotherms and streamlines for different power-law indexes at $Da = 10^{-4}$, $Ra = 10^{6}$, $Pr = 0.1$, and $\epsilon = 0.4$. It is observed that the convection process enhances as the power-law index rises in the studied Darcy number. Fig.6 exposes the local temperature, and the vertical velocity at Y = 0.5 and the local Nusselt number on the hot wall for different power-law indexes at $Da = 10^{-2}$, $Ra = 10^{5}$, and $\epsilon = 0.4$. The temperature profile becomes linear when the power-law index drops which clarifies the power-law index effect for the increase in the convection process evidently. In addition, the velocity magnitude enhances significantly with the increase in the power-law index. The local Nusselt number rises with the enhancement of power-law index. In fact, for low values of power-law index, the viscous force more readily overcomes the buoyancy force and as a result of this, no significant flow is induced within the enclosure. Table 4 confirms this trend where the average Nusselt number augments due to the increase in power-law index.

Figs. 7 display the isotherms, and streamlines clearly for various porosities at

$n = 1.2$, $Pr = 0.1$, $Da = 10^{-2}$, and $Ra = 10^4$. It illustrates that the gradient of the isotherms on the hot wall decreases as the porosity decreases. The trend has been confirmed by the streamlines as the core of them demonstrates the convection process decreases with the drop of the porosity. Fig.8 indicates the local temperature, and the vertical velocity at Y = 0.5 and the local Nusselt number on the hot wall for different porosities at $n = 1.2$, $Pr = 0.1$, $Da = 10^{-2}$, and $Ra = 10^4$. It is evident that the effect of porosity on the local Nusselt number is significant where the increase in porosity enhances the local Nusselt number steadily and therefore rises the convection process. The vertical velocities distributions in the middle of the cavity indicate the growth of porosity enhances the velocity in the cavity drastically. It demonstrates that the development of convection, which increases at higher porosities, causes the temperature in the middle of the cavity to augment markedly. Tables 5 state average Nusselt numbers in different porosities for various Rayleigh, power-law indexes and Darcy numbers. It demonstrates that the average Nusselt number enhances as the porosity increases gradually in different studied parameters.

Bingham fluids form a special sub-class of non-Newtonian fluids in which the flow field is divided into two regions: the first is an unyielded zone where the fluid is at rest or undergoes a rigid motion, and the second where the fluid flows like a viscous liquid. In the unyielded zone, the stress is less than or equal to a critical value, the yield stress, and in the yielded region, the stress exceeds the yield stress. Bingham [27] constituted the fluids as follows:

$$\begin{cases} \mathbf{A_1} = \mathbf{0}, & |\tau| \le \tau_y, \\ \boldsymbol{\tau} = \left(\eta_p + \frac{\tau_y}{\dot{\gamma}}\right)\mathbf{A_1}, & |\tau| > \tau_y, \end{cases} \tag{3.42}$$

The plastic viscosity $\eta_p$ and the yield stress $\tau_y$ are constant, and the the invariant $|\tau|$ is defined below:

$$|\tau| = \frac{1}{\sqrt{2}}\sqrt{\boldsymbol{\tau} : \boldsymbol{\tau}}. \tag{3.43}$$

In 1987, Papanastasiou [28] proposed an exponential regularization for the Bingham equation by introducing the time–dimension parameter $m$ which controls the exponential growth of stress. It is well known that the absence of a constitutive relation which applies throughout the flow has led to approximate models such as the Papanastasiou and the bi-viscosity models. In the Papanastasiou model, which is of interest here, the constitutive equation for the incompressible Bingham fluid is replaced by that of a material with a non-Newtonian viscosity. That is,

$$\boldsymbol{\tau} = \eta(\dot{\gamma})\mathbf{A}_1, \tag{3.44}$$

where

$$\eta(\dot{\gamma}) = \eta_p + \frac{\tau_y}{\dot{\gamma}}\left[1 - \exp(-m\dot{\gamma})\right], \quad (3.45)$$

where $m > 0$ is the parameter which can be chosen. Note that the viscosity function in Eq.(3.45) is a smooth function of its argument. As far as numerical modelling is concerned, one can employ Eq.(3.45) and choose an appropriate value for the parameter $m$. It is generally believed that increasing the value of the parameter $m$ will bring the predictions of the Papanastasiou model closer to that of the exact Bingham model. As shown by Glowinski [32], for the solution $u_e$ of the regularised model to be a good approximation to the exact solution u, the regularisation parameter $\pi$ has to be small; for our purposes, one can take $\pi = 1/m$. However, when this parameter is small, the initial/boundary value problem is badly conditioned whenever the unyielded zone is large. Since an increase in the Bingham number results in a larger unyielded zone, it is clear that increasing the value of m may not provide quantitatively accurate results However, as shown in Figs. 7 and 8 in Kefayati and Huilgol [33], increasing $m$ from 100 to 1000 when Bn = 10 and 1 does not produce any significant improvement in the predictions of the regularised model as far as the yielded/unyielded regions are concerned. Similar observations regarding the streamlines and the isotherms can be made as seen in Figs. 7 and 8 respectively. Finally, it can be seen in Fig. 15(b) in the Dimakopoulos et al. [34], even when $m = 10^6$, there is a fair amount of divergence as the Bingham number increases. In addition, Kefayati and Huilgol [33] demonstrated for the case of mixed convection of Bingham fluids, the results of the Papanastasiou model at $m = 1000$ and the exact Bingham model are nearly the same. So, we fix the parameter at $m = 1000$. The non-dimensional effective stress tensor and the effective dynamic viscosity following the Papanastasiou model is as [29]

$$\eta(\dot{\gamma}) = 1 + \frac{Bn}{\dot{\gamma}}\left[1 - \exp(-m\dot{\gamma})\right], \quad (3.46)$$

$Bn$ is the Bingham number and is defined $Bn = \frac{\tau_y L}{\eta U}$.

The results of a Bingham fluid undergoing natural convection in an enclosure have been compared with the work of Turan et al. [30] and Huigol and Kefayati [31] in Table 6 and demonstrates a good agreement.

Fig.9 depicts the isotherms, streamlines, and yielded/unyielded sections for different Bingham numbers at $Da = 10^{-4}$, $Ra = 10^6$, $Pr = 0.1$, and $\epsilon = 0.4$. It shows that the curved shape of the isotherm declines with the rise of Bingham number. The process causes the gradient of temperature on the hot wall to drop and therefore heat transfer decreases with the rise of Bingham number. The streamlines can prove the decrease in the convection process with the growth of Bingham number as the inclined elliptical form of the core of the cavity alters to a circular shape. As a result, the convection process decreases with the enhancement of Bingham number. The unyielded sections occupy more spaces in the cavity as the Bingham number augments. In fact, the rise of Bingham number causes the yielded regions to remove gradually. Table 7 verifies this pattern as the average Nusselt number decreases with the rise of Bingham number. There is a Bingham number which the flow would be fully unyielded. The value is named as critical Bingham number ($Bn_c$) and is specified.

Fig.10 displays the isotherms, streamlines, and the yielded and unyielded zones clearly for various porosities in a fixed Bingham number. It illustrates that the gradient of the isotherms on the hot wall decreases as the porosity decreases. The trend has been confirmed by the streamlines as the core of them demonstrates the convection process decreases with the drop of the porosity. Further, it exhibits that the unyielded section for a certain Bingham and Rayleigh numbers increases with the drop of porosity. In fact, the increment of the unyielded sections at lower porosity causes the heat transfer to drop.

Fig.11 indicates the vertical velocity and the local Nusselt number for different porosities at $Da = 10^{-2}$, $Ra = 10^5$, and $Bn = 2$. It is evident that the effect of porosity on the local Nusselt number is significant where the increase in porosity enhances the local Nusselt number steadily and therefore rises the convection process. The vertical velocities distributions in the middle of the cavity indicate the growth of porosity enhances the velocity in the cavity drastically. It demonstrates that the development of the unyielded sections, which increases at higher porosities, causes the velocities augment markedly.

Table 8 states average Nusselt numbers in different porosities. It demonstrates that the average Nusselt number enhances as the porosity increases gradually in different studied parameters.

## 4 Summary

In this paper, a general thermal lattice Boltzmann method is introduced for non-Newtonian fluid flows in porous media at the REV scale. This approach has the ability to be applied to all fluids, whether they be Newtonian, or power law fluids, or viscoelastic and viscoplastic fluids. The derivation includes all parameters in energy equations e.g. the viscous dissipation and the external supply. To validate the accuracy of the method, natural convection in a porous cavity filled with a Newtonian fluid was studied and compared with previous studies. In addition, natural convection of power-law fluids in a wide range of power-law indexes (shear thinning($n < 1$), shear thickening ($n > 1$)) was studied and demonstrated a different manner in comparison with a pure fluid against the power-law index in the porous cavity. In other words, the convection process enhances by the rise of power-law index. At the end, the effect of porosity in natural convection of power-law fluid in a porous cavity was investigated and demonstrated the convection process strengthens due to the rise of porosity. Finally, the method was utilised to simulate the viscoplastic porous material on natural convection while the yielded/unyielded sections were illustrated in different Bingham numbers. The increase in Bingham number decreases heat transfer as it augments the unyielded sections. The unyielded regions decrease with the augmentation of porosity for certain Rayleigh and Bingham numbers. The heat transfer increases as the porosity rises.

# Appendix A

Substituting the expression for $f_\alpha$ in (2.9) into (2.8), we find that

$$\frac{\partial f_\alpha^{eq}}{\partial t} + \boldsymbol{\xi}_\alpha \cdot \nabla_{\mathbf{x}} f_\alpha^{eq} - F_\alpha = -\frac{1}{\tau} f_\alpha^{(1)} + O(\varepsilon). \tag{A1}$$

Since the velocity vectors $\boldsymbol{\xi}_\alpha$ do not depend on the spatial coordinates, one sees that

$$\nabla \cdot (f_\alpha^{eq} \boldsymbol{\xi}_\alpha) = \boldsymbol{\xi}_\alpha \cdot \nabla_{\mathbf{x}} f_\alpha^{\mathrm{eq}}. \tag{A2}$$

Hence, (A1) can be rewritten as

$$\frac{\partial f_\alpha^{eq}}{\partial t} + \nabla \cdot (f_\alpha^{eq} \boldsymbol{\xi}_\alpha) - F_\alpha = -\frac{1}{\tau} f_\alpha^{(1)} + O(\varepsilon). \tag{A3}$$

Summing the equation above, we obtain

$$\frac{\partial}{\partial t}\left( \sum_{\alpha=0}^{8} f_\alpha^{eq} \right) + \nabla \cdot \left( \sum_{\alpha=0}^{8} f_\alpha^{eq} \boldsymbol{\xi}_\alpha \right) - \sum_{\alpha=0}^{8} F_\alpha = -\frac{1}{\tau} \sum_{\alpha=0}^{8} f_\alpha^{(1)} + O(\varepsilon). \tag{A4}$$

We have the following condition for the body force (Guo and Zhao [10])

$$\sum_{\alpha=0}^{8} F_\alpha = 0, \tag{A5}$$

Appealing to (2.11), (2.12), (2.13) and recalling that $\rho$ is a constant, the above equation reduces to

$$\rho(\nabla \cdot \mathbf{u}) = 0 + O(\varepsilon), \tag{A6}$$

or the continuity equation for an incompressible medium is satisfied.

Next,

$$\nabla \cdot (f_\alpha^{eq} \boldsymbol{\xi}_\alpha \otimes \boldsymbol{\xi}_\alpha) = (\boldsymbol{\xi}_\alpha \cdot \nabla_{\mathbf{x}} f_\alpha^{\mathrm{eq}}) \boldsymbol{\xi}_\alpha. \tag{A7}$$

We have the following condition for the body force (Guo and Zhao [10])

$$\sum_{\alpha=0}^{8} F_\alpha \boldsymbol{\xi}_\alpha = \mathbf{f}, \tag{A8}$$

Hence, multiplying (A1) throughout by $\boldsymbol{\xi}_\alpha$, summing over $\alpha$, and appealing to (2.11) - (2.15), one obtains

$$\frac{\rho}{\epsilon} \frac{\partial \mathbf{u}}{\partial t} + \nabla \cdot \mathbf{M} - \mathbf{f} = \mathbf{0} + O(\varepsilon). \tag{A9}$$

Rearranging, one obtains the equations of motion for an incompressible porous fluid:

$$\rho\mathbf{a} + \frac{1}{\epsilon}\nabla(\epsilon p) - \frac{1}{\epsilon}\nabla\cdot\boldsymbol{\tau} - \mathbf{f} = \mathbf{0} + O(\varepsilon), \quad \mathbf{a} = \frac{1}{\epsilon}\frac{\partial\mathbf{u}}{\partial t} + \frac{1}{\epsilon^2}(\mathbf{u}\cdot\nabla)\mathbf{u}. \qquad \text{(A10)}$$

Thus, the set of equations (2.11) - (2.22) deliver momentum's equations for an incompressible porous medium.

# Appendix B

Here, we shall discuss the stability of the numerical scheme. Finding the parameter $\sigma$, we multiply $f_{\alpha}^{eq}$ with $|\boldsymbol{\xi}_{\alpha}|^2/2$ and take the sum, which leads to

$$\sum_{\alpha=0}^{8} \frac{1}{2} f_{\alpha}^{eq} |\boldsymbol{\xi}_{\alpha}|^2 = p + \frac{1}{2}\rho \left|\mathbf{u}/\epsilon\right|^2 , \tag{B1}$$

Next, it is easy to verify that

$$\sum_{\alpha=0}^{8} F_{\alpha} |\boldsymbol{\xi}_{\alpha}|^2 = 0. \tag{B2}$$

Hence,

$$\frac{\partial}{\partial t}\left[p + \frac{1}{2}\rho|\mathbf{u}/\epsilon|^2\right] + \frac{\sigma^2}{2}\rho(\nabla \cdot \mathbf{u}) = O\left(\lambda\right). \tag{B3}$$

The Courant-Friedrichs-Lewy (CFL) condition states that [35,36]

$$K = \frac{u\Delta t}{\Delta x} + \frac{v\Delta t}{\Delta y} \leq 1. \tag{B4}$$

This can be used in (B3) and we obtain

$$\left[|\mathbf{u}/\epsilon|^2 + \frac{2p}{\rho}\right] + \sigma^2 K = O\left(\lambda\right). \tag{B5}$$

Thus, the lattice speed $\sigma$ must satisfy

$$\sigma = K_c \sqrt{\left|\frac{-2p}{\rho} - |\mathbf{u}/\epsilon|^2\right|}\,, \qquad K_c = \frac{1}{\sqrt{K}} \geq 1. \tag{B6}$$

# Appendix C

$$\frac{\partial g_\alpha}{\partial t} + \boldsymbol{\xi}_\alpha \cdot \nabla_{\mathbf{x}} g_\alpha - G_\alpha = -\frac{1}{\varepsilon \tau}(g_\alpha - g_\alpha^{eq}). \tag{C1}$$

Summing Eq. (C1) over all $\alpha$, and using (2.25) - (2.35), one finds that

$$\rho \frac{de}{dt} + \rho \frac{\partial \mathbf{u}}{\partial t} \cdot \mathbf{s} + \nabla \cdot \left( \sum_{\alpha=0}^{8} g_\alpha^{eq} \boldsymbol{\xi}_\alpha \right) - \rho \mathbf{f} \cdot \mathbf{u} = 0 + O(\varepsilon). \tag{C2}$$

Next,

$$\nabla \cdot \left( \epsilon\, p + \rho e + \frac{1}{2}\rho |\mathbf{s}\, \mathbf{u}| \right) \mathbf{s} = \left( \nabla(\epsilon\, p) + \rho \nabla e + \rho(\mathbf{u} \cdot \nabla)\mathbf{s} \right) \cdot \mathbf{s}, \tag{C3}$$

Noting the symmetry of the stress tensor, we have

$$\nabla \cdot (\boldsymbol{\tau} \mathbf{s}) = (\nabla \cdot \boldsymbol{\tau}) \cdot \mathbf{s} + \frac{1}{2} \boldsymbol{\tau} : \mathbf{A}_1. \tag{C4}$$

Combining all of the above and substition of $\mathbf{u} = \epsilon \mathbf{s}$ we obtain

$$\rho \frac{de}{dt} + \left( \rho \mathbf{a} + \frac{1}{\epsilon} \nabla(\epsilon\, p) - \frac{1}{\epsilon} \nabla \cdot \boldsymbol{\tau} - \rho \mathbf{f} \right) \cdot \mathbf{u} - \frac{1}{2} \boldsymbol{\tau} : \mathbf{A}_1 + \nabla \cdot \mathbf{q} - \rho r = 0 + O(\varepsilon), \tag{C5}$$

The equation in parentheses in (C5) according to the Eq. (A10) is equal to zero and demonstrates the momentum equation, so (C5) satisfies the Eq.(2.28).

## References

[1] R.R. Huilgol, GH.R. Kefayati, From mesoscopic models to continuum mechanics: Newtonian and non-newtonian fluids, Journal of Non-Newtonian Fluid Mechanics 233 (2016) 146–154.

[2] R. R. Huilgol, GH. R. Kefayati, A particle distribution function approach to the equations of continuum mechanics in Cartesian, cylindrical and spherical coordinates: Newtonian and non-Newtonian Fluids, Journal of Non-Newtonian Fluid Mechanics 251 (2018) 119–131.

[3] Taha Sochi, Non-Newtonian flow in porous media, Polymer 51 (2010) 5007–5023.

[4] D.A. Nield, A. Bejan, Convection in Porous Media, third ed., vol. XXIV, Springer, 2006.

[5] K. Vafai, Handbook of Porous Media, Marcel Dekker, New York, 2005.

[6] P. Le Quere, T. Alziary de Roquefort, Computation of natural convection in two dimensional cavities with Chebyshev polynomials, J. Comput. Phys. 57 (1985) 210–228.

[7] P. Le Quere, Accurate solutions to the square thermally driven cavity at high Rayleigh number, Comp. Fluids 20 (1991) 29–41.

[8] P. Nithiarasu, K. N. Seetharamu, and T. Sundararajan, Natural Convection Heat Transfer in a Fluid Saturated Variable Porosity Medium, Int. J. Heat Mass Transfer, 40 (1997) 3955–3967.

[9] P. Nithiarasu and K. Ravindran, A New Semi-implicit Time Stepping Procedure for Buoyancy Driven Flow in a Fluid Saturated Porous Medium, Comput. Meth. Appl. Mech. Eng., 165 (1998) 147–154.

[10] Zhaoli Guo , T. S. Zhao, A lattice Boltzmann model for convection heat transfer in porous media, Numerical Heat Transfer, Part B, 47 (2005) 157–177.

[11] Qing Liu, Ya-Ling He, Qing Li, Wen-Quan Tao, A multiple-relaxation-time lattice Boltzmann model for convection heat transfer in porous media, International Journal of Heat and Mass Transfer 73 (2014) 761–775.

[12] Liang Wang, Jianchun Mi, Zhaoli Guo, A modified lattice Bhatnagar–Gross–Krook model for convection heat transfer in porous media, International Journal of Heat and Mass Transfer 94 (2016) 269–291.

[13] Debayan Das, Pratibha Biswal, Monisha Roy, Tanmay Basak, Role of the importance of 'Forchheimer term' for visualization of natural convection in porous enclosures of various shapes, International Journal of Heat and Mass Transfer 97 (2016) 1044–1068.

[14] Debayan Das, Tanmay Basak, Role of discrete heating on the efficient thermal management within porous square and triangular enclosures via heatline approach, International Journal of Heat and Mass Transfer 112 (2017) 489–508.

[15] S.C. Fu, R.M.C. So, R.M.C. Leung, Linearized-Boltzmann-type-equation-based finite difference method for thermal incompressible flow, Comput. Fluids 6 (2012) 67–80.

[16] U. Frisch, B. Hasslacher, Y. Pomeau, Lattice gas automata for the navier-stokes equation, Phys. Rev. Lett. 56 (1986) 1505–1508.

[17] U. Frisch, D. d'Humères, B. Hasslacher, P. Lallemand, Y. Pomeau , J.-P. Rivet , Lattice gas hydrodynamics in two and three dimensions, Complex Syst. 1 (1987) 649–707.

[18] S. Wolfram, Cellular automaton fluids 1: basic theory, J. Stat. Phys. 45 (1986) 471–526.

[19] Shiyi Chen, Gary D. Doolen, Lattice Boltzmann method for fluid flows, Annu. Rev. Fluid Mech. 1998 (30) 329–64.

[20] P. L. Bhatnagar, E. P. Gross, M. Krook, A model for collision processes in gases. I. Small amplitude processes in charged and neutral one-component systems. Phys. Rev. Ser. 2, 94 (1954), 511–525.

[21] S. Chen, Z. Wang, X. W. Shan, G. D. Doolen, Lattice Boltzmann computational fluid dynamics in three dimensions. J. Stat. Phys. 68 (1992) 379–400.

[22] Y. H. Qian, D. d'Humi'eres, P. Lallemand, Lattice BGK models for Navier-Stokes equation.Europhys. Lett. 17 (1992) 479–484.

[23] E. F. Toro, Riemann Solvers and Numerical Methods for Fluid Dynamics: A Practical Introduction. Springer, 1999, pp. 531–542.

[24] P. D. Lax, B. Wendroff, Systems of conservation laws, Comm. Pure Appl. Math. 13 (1960) 217–237.

[25] L. Khezzar, D. Siginer, I. Vinogradov, Natural convection of power law fluids in inclined cavities, Int. J. Therm. Sci. 53 (2012) 8–17.

[26] G. B. Kim, J. M. Hyun, H. S. Kwak, Transient buoyant convection of a power-law non-Newtonian fluid in an enclosure, Int. J. Heat Mass Transfer 46 (2003) 3605–3617.

[27] E. C. Bingham, Fluidity and plasticity, McGraw-Hill, New York (1922).

[28] T.C. Papanastasiou, Flow of materials with yield, J. Rheol. 31 (1987) 385–404.

[29] G.H.R. Kefayati, Double-diffusive natural convection and entropy generation of Bingham fluid in an inclined cavity, International Journal of Heat and Mass Transfer 116 (2018) 762–812.

[30] O. Turan, N. Chakraborty, R.J. Poole, Laminar natural convection of Bingham fluids in a square enclosure with differentially heated side walls, J. Non- Newton. Fluid Mech. (2010) 165 901–913.

[31] R.R. Huilgol, GH.R. Kefayati, Natural convection problem in a Bingham fluid using the operator-splitting method, Journal of Non-Newtonian Fluid Mechanics 220 (2015) 22-32.

[32] R. Glowinski, Finite element methods for incompressible viscous flow, in: Handbook of Numerical Analysis, 9 (2003) 3–1176.

[33] G.H.R. Kefayati, R.R. Huilgol, Lattice Boltzmann Method for simulation of mixed convection of a Bingham fluid in a lid-driven cavity, International Journal of Heat and Mass Transfer 103 (2016) 725–743.

[34] M. Dimakopoulos, M. Pavlidis, J. Tsamopoulos, Steady bubble rise in Herschel–Bulkley fluids and comparisons of predictions via the Augmented Lagrangian Method with those via the Papanastasiou model, J. Non-Newt. Fluid Mech. 200 (2013) 34–51.

[35] J. Blazek, Computational Fluid Dynamics: Principles and Applications. Elsevier, 2001, pp. 347–350.

[36] T. Cebeci, J. P. Shao, F. Kafyeke, E. Laurendeau, Computational Fluid Dynamics for Engineers. Springer, 2005, pp. 311–320.

Table 1
Grid independence study at $Ra = 10^5$, $Da = 10^{-2}$, and $\epsilon = 0.4$

| Mesh size | $Nu_{avg}$ |
|---|---|
| 100*100 | 3.028 |
| 120*120 | 3.021 |
| 130*130 | 3.014 |
| 140*140 | 3.011 |
| 150*150 | 3.010 |
| 160*160 | 3.010 |

Table 2
Comparison of the average Nusselt number for different Rayleigh and Darcy numbers at $\epsilon = 0.4$, and $Pr = 1$

| | $Ra$ | Ref [8] | Ref [10] | Ref [11] | Ref [12] | Present study |
|---|---|---|---|---|---|---|
| $Da = 10^{-2}$ | | | | | | |
| | $10^3$ | 1.010 | 1.008 | 1.007 | 1.008 | 1.008 |
| | $10^4$ | 1.408 | 1.367 | 1.362 | 1.365 | 1.366 |
| | $10^5$ | 2.983 | 2.998 | 3.009 | 3.012 | 3.010 |
| $Da = 10^{-4}$ | | | | | | |
| | $10^5$ | 1.067 | 1.066 | 1.067 | 1.067 | 1.067 |
| | $10^6$ | 2.550 | 2.603 | 2.630 | 2.618 | 2.612 |
| | $10^7$ | 7.810 | 7.788 | 7.808 | 7.811 | 7.809 |
| $Da = 10^{-6}$ | | | | | | |
| | $10^7$ | 1.79 | 1.077 | 1.085 | 1.089 | 1.081 |
| | $10^8$ | 2.970 | 2.955 | 2.949 | 3.014 | 2.998 |
| | $10^9$ | 11.460 | 11.395 | 11.610 | 11.733 | 11.512 |

Table 3
Comparison between present and previous studies for power-law fluids by the normalized average Nusselt number ($\frac{\mathrm{Nu_{avg}}(n)}{\mathrm{Nu_{avg}}(n=1)}$)) at Pr = 100.

| | n | Ref [25] | Ref [26] | Present study |
|---|---|---|---|---|
| $Ra = 10^4$ | | | | |
| | n = 0.6 | 1.04 | - | 1.05 |
| | n = 0.7 | 1.03 | - | 1.04 |
| | n = 0.8 | 1.02 | - | 1.03 |
| | n = 0.9 | 1.01 | - | 1.02 |
| | n = 1 | 1 | - | 1 |
| | n = 1.1 | 0.99 | - | 0.98 |
| | n = 1.2 | 0.97 | - | 0.96 |
| | n = 1.3 | 0.95 | - | 0.94 |
| | n = 1.4 | 0.93 | - | 0.92 |
| $Ra = 10^5$ | | | | |
| | n = 0.6 | 1.48 | 1.46 | 1.49 |
| | n = 0.7 | 1.30 | 1.28 | 1.32 |
| | n = 0.8 | 1.18 | 1.17 | 1.19 |
| | n = 0.9 | 1.09 | 1.08 | 1.10 |
| | n = 1 | 1 | 1 | 1 |
| | n = 1.1 | 0.93 | - | 0.92 |
| | n = 1.2 | 0.89 | - | 0.88 |
| | n = 1.3 | 0.86 | - | 0.85 |
| | n = 1.4 | 0.82 | - | 0.81 |

Table 4
Comparison of the average Nusselt number on the hot wall in different power-law indexes at $\epsilon = 0.4$, $Pr = 0.1$, $Da = 10^{-4}$, and $Ra = 10^6$

| n (Power-law index) | $Nu_{avg}$ |
|---|---|
| n = 0.4 | 1.0937 |
| n = 0.6 | 1.2858 |
| n = 0.8 | 1.5885 |
| n = 1 | 1.9851 |
| n = 1.2 | 2.1770 |
| n = 1.4 | 2.3118 |
| n = 1.6 | 2.3686 |

Table 5
Comparison of the average Nusselt number on the hot wall in different porosities at $n = 1.2$, $Pr = 0.1$, $Da = 10^{-2}$, and $Ra = 10^4$

| $\epsilon$ (Porosity) | $Nu_{avg}$ |
|---|---|
| $\epsilon = 0.1$ | 1.0318 |
| $\epsilon = 0.2$ | 1.0806 |
| $\epsilon = 0.4$ | 1.1994 |
| $\epsilon = 0.6$ | 1.3167 |
| $\epsilon = 0.8$ | 1.4170 |

Table 6
Comparison between present and previous studies for Bingham fluids by the the average Nusselt number at the hot wall in different Rayleigh numbers for Pr = 1.

| | Bn | Ref [30] | Ref [31] | Present study |
|---|---|---|---|---|
| $Ra = 10^4$ | | | | |
| | Bn = 0 | 2.23 | 2.23 | 2.23 |
| | Bn = 0.5 | 2.00 | 1.91 | 1.95 |
| | Bn = 1 | 1.70 | 1.65 | 1.68 |
| | Bn = 1.5 | 1.43 | 1.49 | 1.45 |
| | Bn = 2 | 1.21 | 1.34 | 1.30 |
| | Bn = 2.5 | 1.10 | 1.21 | 1.18 |
| | Bn = 3 | 1.00 | 1.10 | 1.05 |
| $Ra = 10^5$ | | | | |
| | Bn = 0 | 4.60 | 4.60 | 4.60 |
| | Bn = 1 | 3.89 | 3.89 | 3.88 |
| | Bn = 2 | 3.45 | 3.46 | 3.44 |
| | Bn = 3 | 2.95 | 3.16 | 3.12 |

Table 7
Comparison of the average Nusselt number on the hot wall in different Bingham numbers ($Bn$) at $\epsilon = 0.4$, $Pr = 0.1$, $Da = 10^{-4}$, and $Ra = 10^6$

| $Bn$ | $Nu_{avg}$ |
|---|---|
| $Bn = 1$ | 2.224 |
| $Bn = 2$ | 2.145 |
| $Bn = 5$ | 1.900 |
| $Bn = 10$ | 1.504 |
| $Bn = 15$ | 1.182 |
| $Bn = 20$ | 1.031 |
| $Bn_c = 22$ | 1.000 |

Table 8
Comparison of the average Nusselt number for different porosities at $Ra = 10^5$, $Da = 10^{-2}$, $Bn = 2$

| $\epsilon = 0.1$ | $\epsilon = 0.2$ | $\epsilon = 0.4$ | $\epsilon = 0.6$ | $\epsilon = 0.8$ | $\epsilon = 0.9$ |
|---|---|---|---|---|---|
| 1.012 | 1.057 | 1.337 | 1.673 | 1.977 | 2.114 |

**List of Figures**

different porosities at $Da = 10^{-2}$, $Ra = 10^5$, and $Bn = 2$

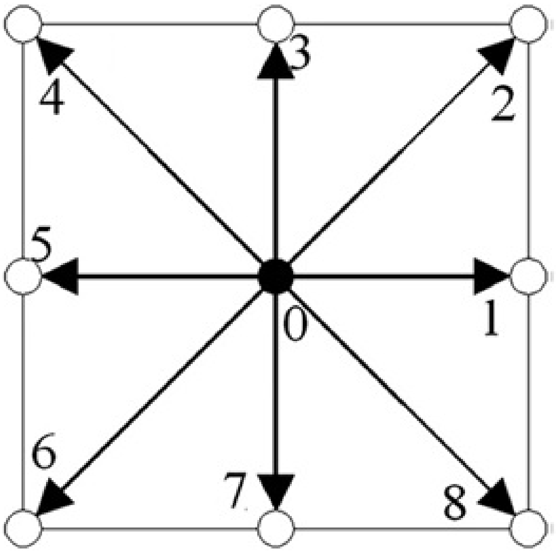

Fig. 1. Discrete velocity distribution in D2Q9

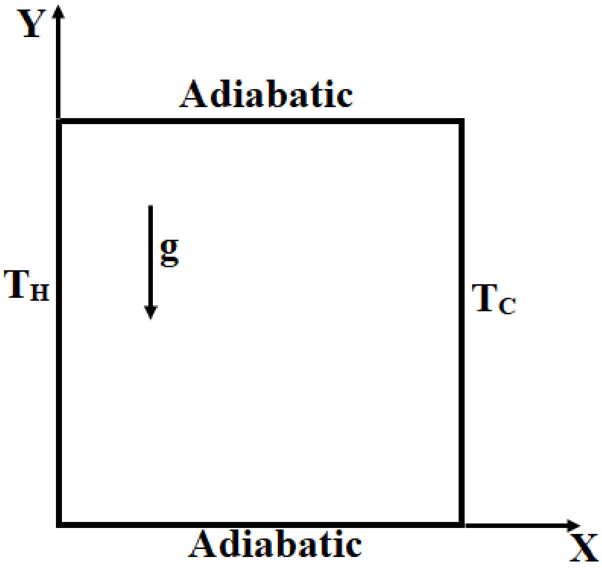

Fig. 2. The geometry of the present problem

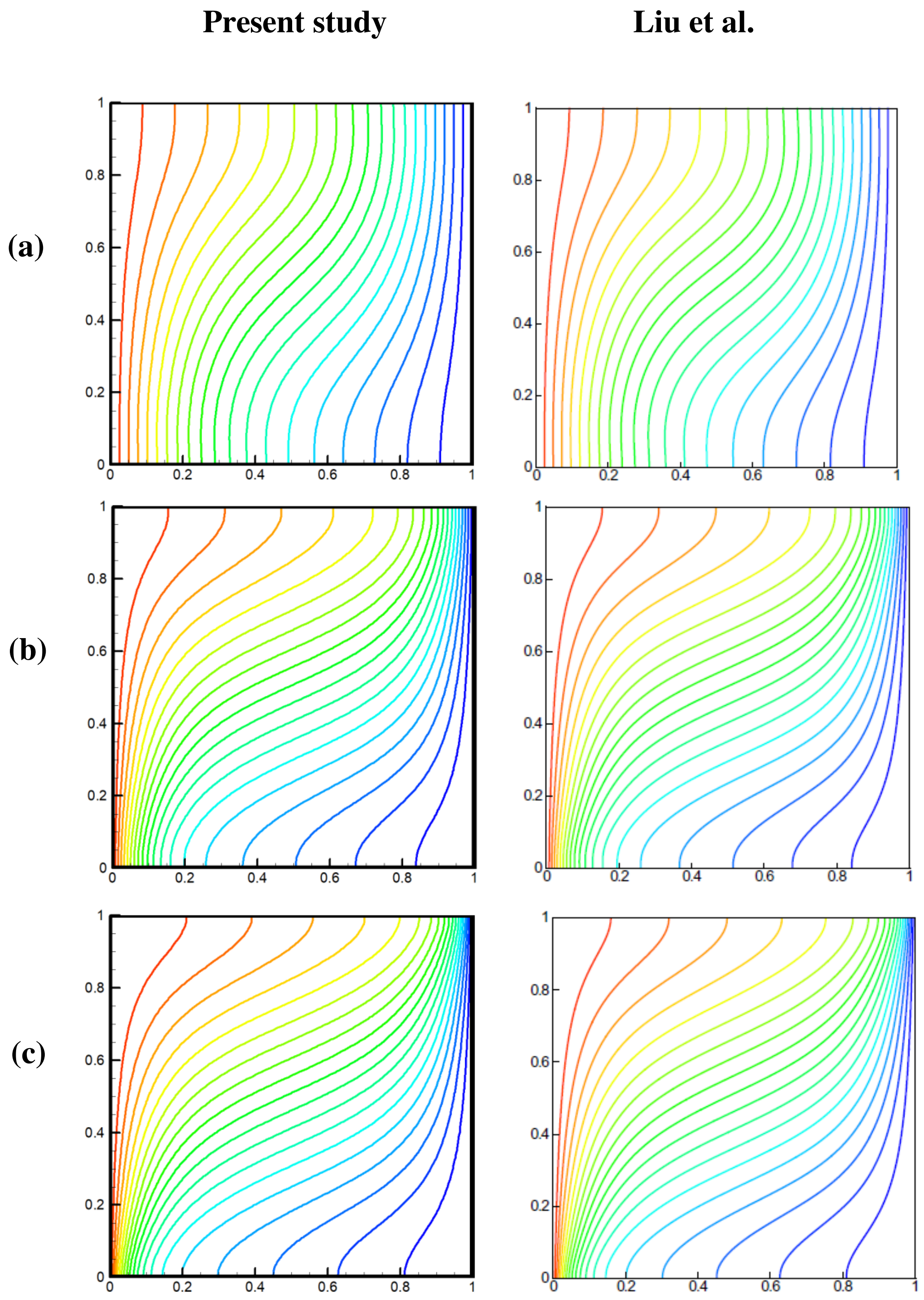

Fig. 3. Comparison of the isotherms between present study and the study of Liu et al. [11] for the porosity $\epsilon = 0.4$, and $Pr = 1$ at (a) $Da = 10^{-2}$, $Ra = 10^4$ (b) $Da = 10^{-4}$, $Ra = 10^6$ (c) $Da = 10^{-6}$, $Ra = 10^8$

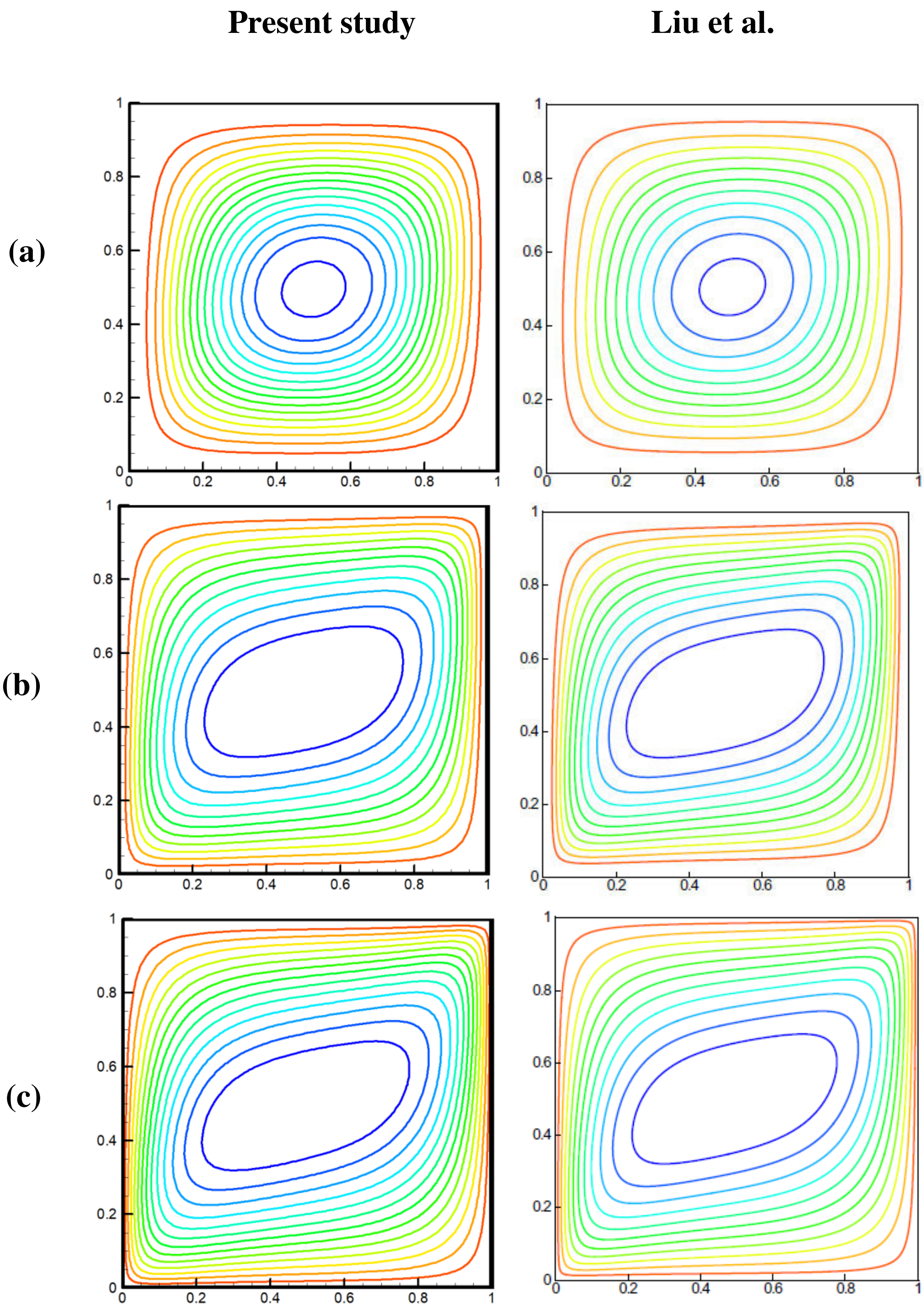

Fig. 4. Comparison of the streamlines between present study and the study of Liu et al. [11] for the porosity $\epsilon = 0.4$, and $Pr = 1$ at (a) $Da = 10^{-2}$, $Ra = 10^{4}$ (b) $Da = 10^{-4}$, $Ra = 10^{6}$ (c) $Da = 10^{-6}$, $Ra = 10^{8}$

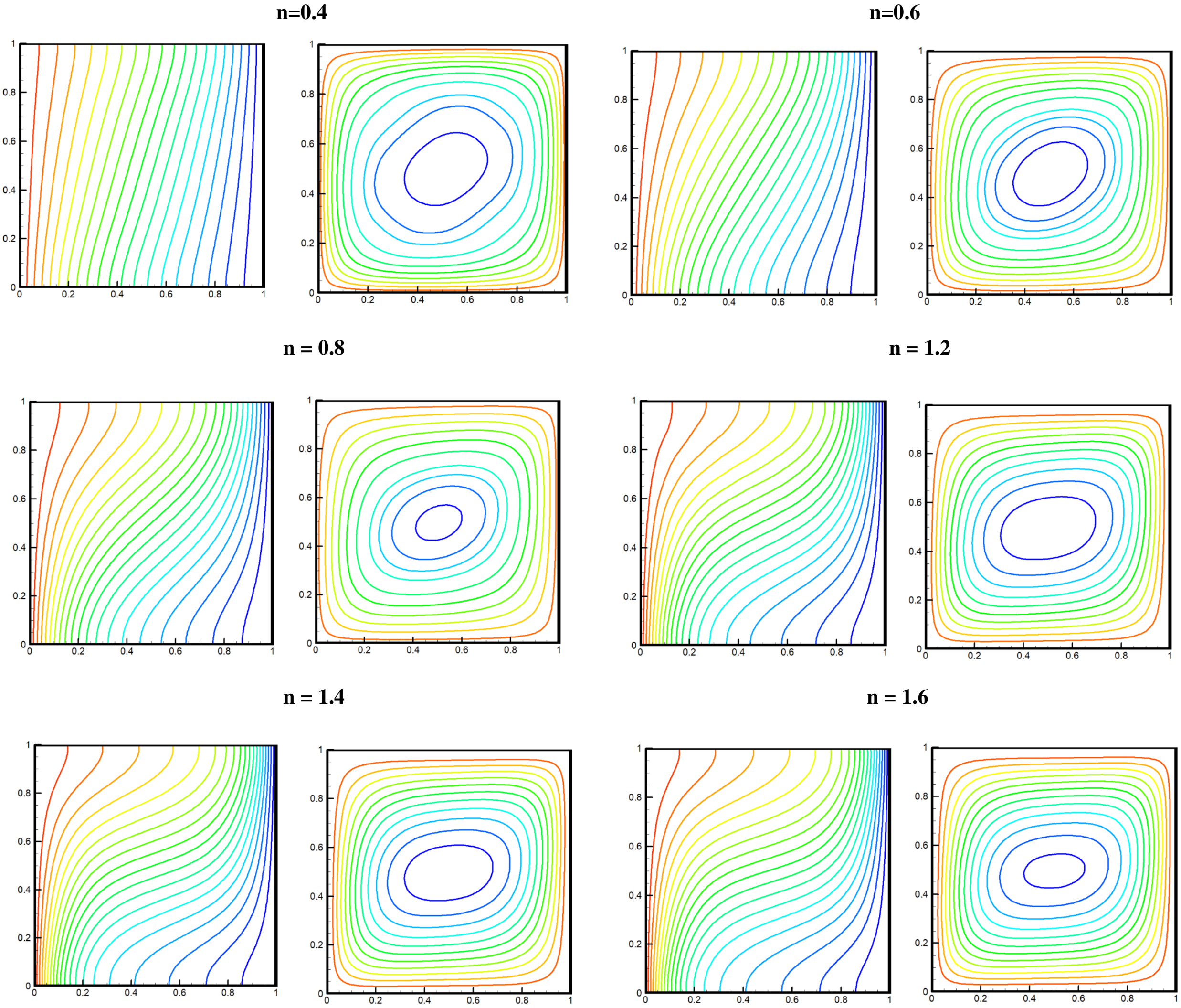

Fig. 5. Comparison of the isotherms (Left) and streamlines (Right) in different power-law indexes at $\epsilon = 0.4$, $Pr = 0.1$, $Da = 10^{-4}$, and $Ra = 10^{6}$

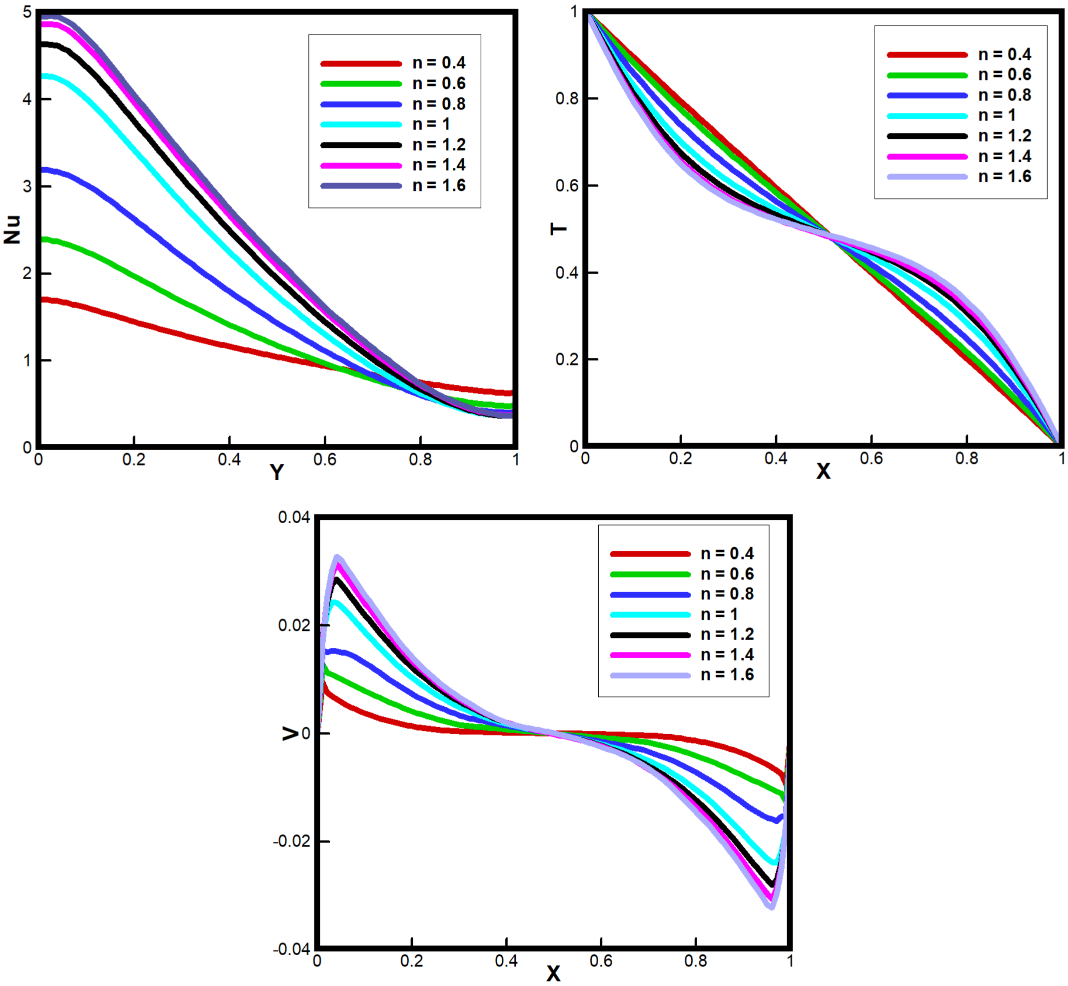

Fig. 6. Comparison of the vertical velocity and temperature at Y = 0.5 and the local Nusselt number on the hot wall in different power-law indexes at $\epsilon = 0.4$, $Pr = 0.1$, $Da = 10^{-4}$, and $Ra = 10^6$

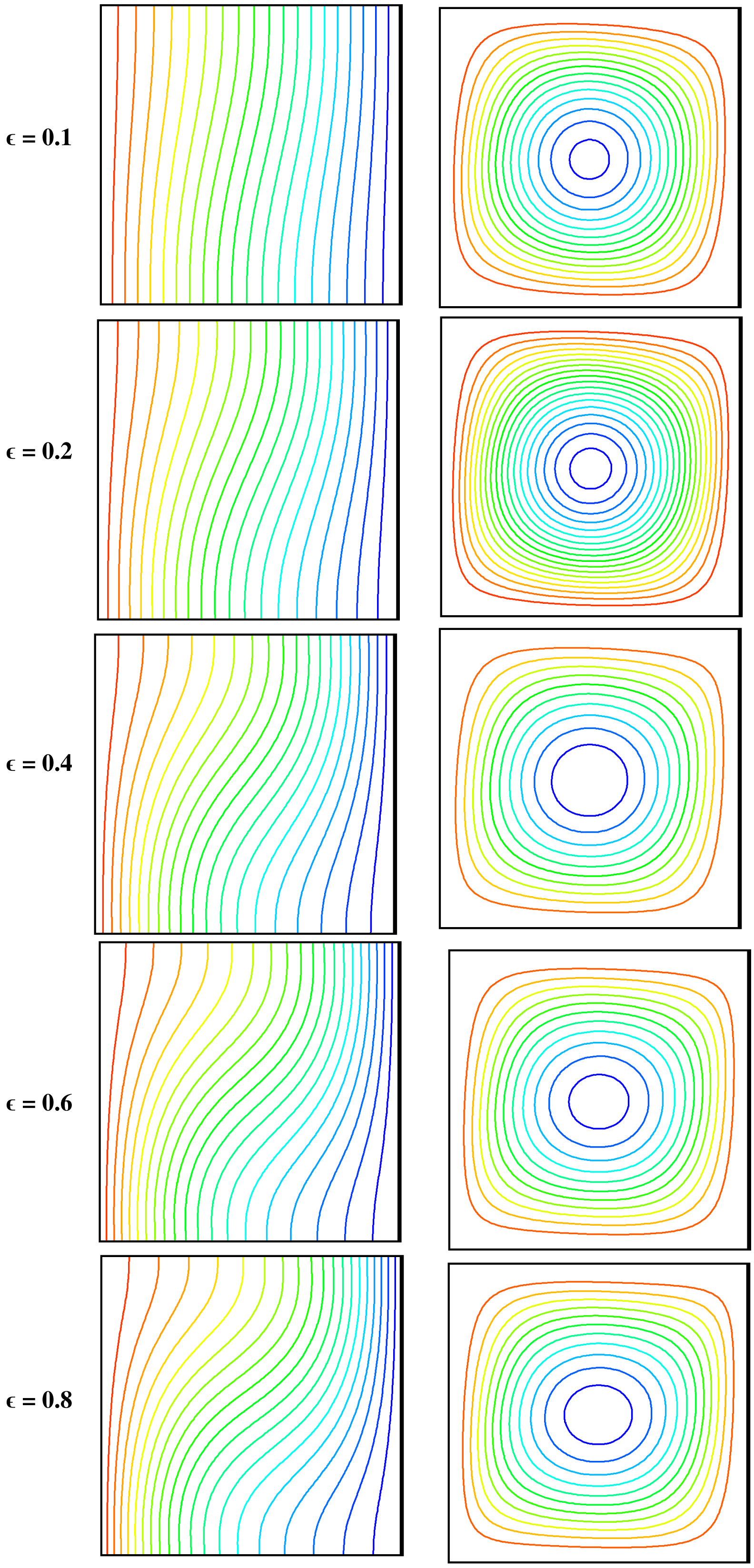

Fig. 7. Comparison of the isotherms (Left) and streamlines (Right) in different porosities at $n = 1.2$, $Pr = 0.1$, $Da = 10^{-2}$, and $Ra = 10^4$

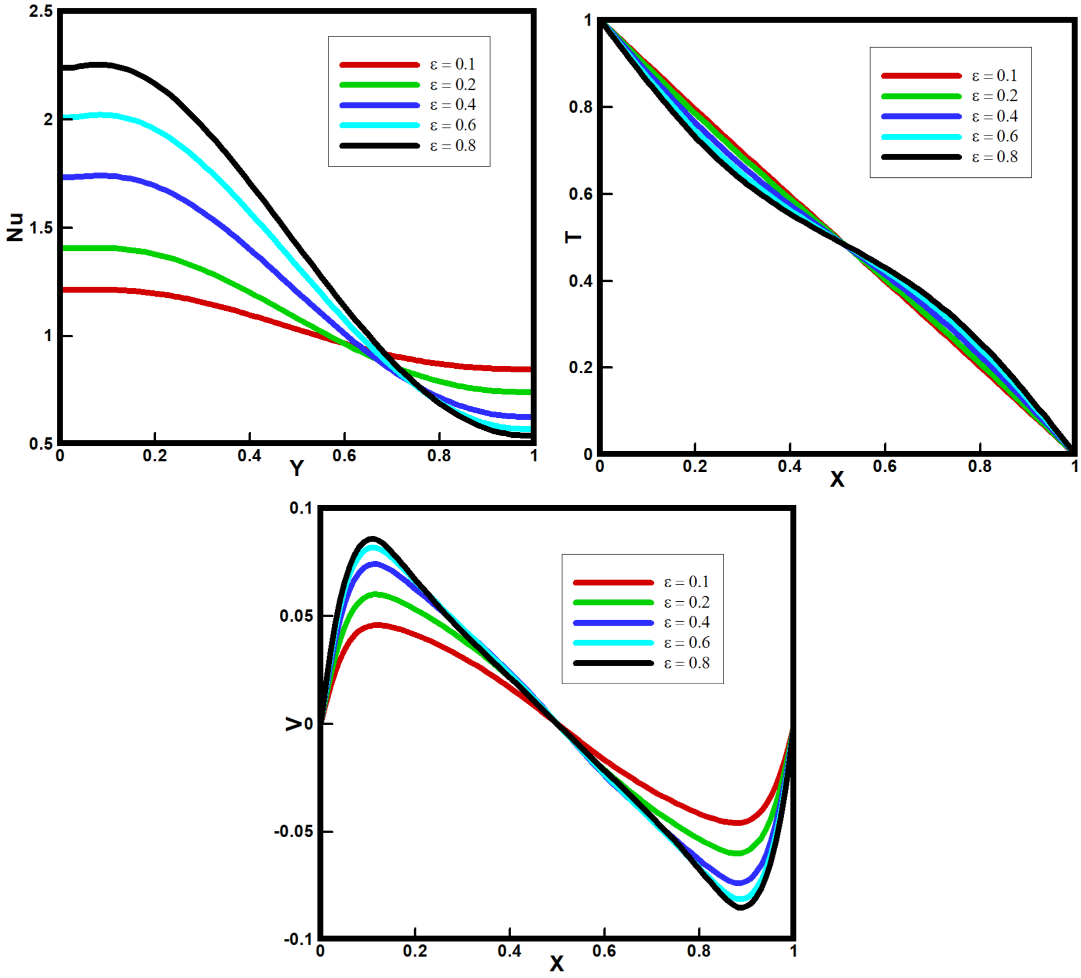

Fig. 8. Comparison of the vertical velocity and temperature at Y = 0.5 and the local Nusselt number on the hot wall in different porosities at $n = 1.2$, $Pr = 0.1$, $Da = 10^{-2}$, and $Ra = 10^4$

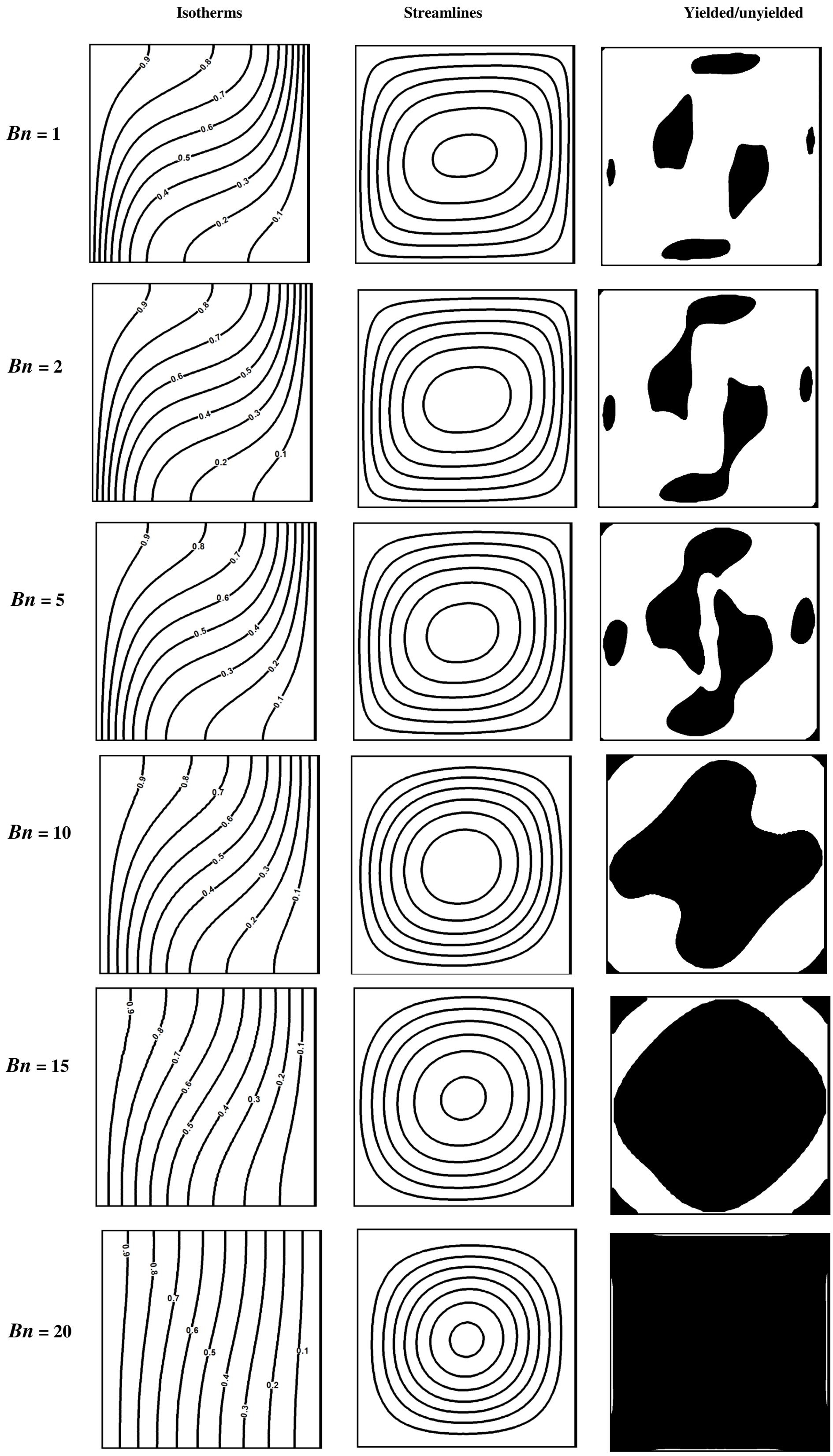

Fig. 9. Comparison of the isotherms and streamlines in different Bingham numbers at $\epsilon = 0.4$, $Pr = 0.1$, $Da = 10^{-4}$, and $Ra = 10^6$

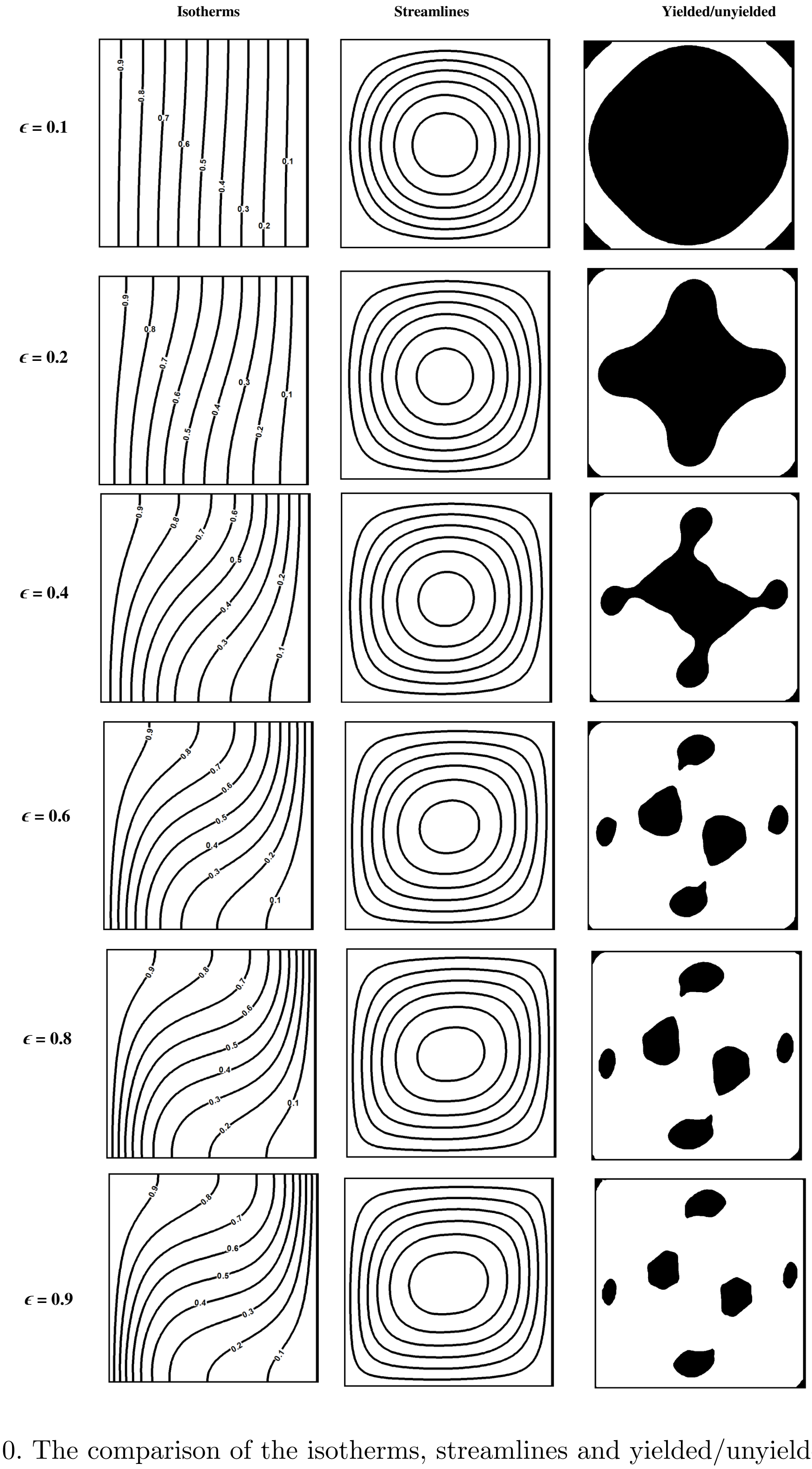

Fig. 10. The comparison of the isotherms, streamlines and yielded/unyielded parts in different porosities at $Da = 10^{-2}$, $Ra = 10^5$, and $Bn = 2$

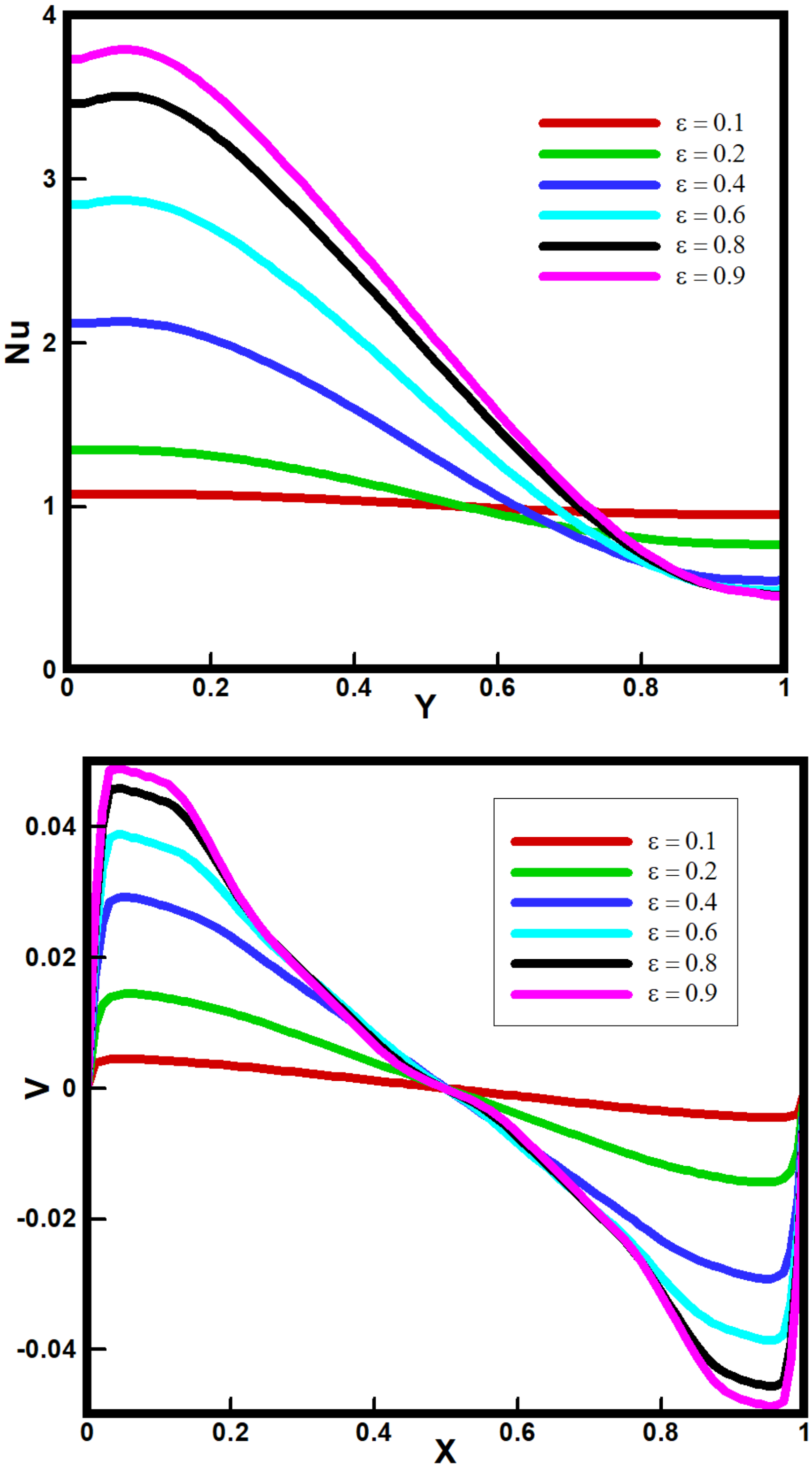

Fig. 11. Comparison of the vertical velocity and the local Nusselt number in different porosities at $Da = 10^{-2}$, $Ra = 10^5$, and $Bn = 2$